JCI The Journal of Clinical Investigation

Spatiotemporal transcriptomic mapping of regenerative inflammation in skeletal muscle reveals a dynamic multilayered tissue architecture

Andreas Patsalos, … , H. Lee Sweeney, Laszlo Nagy

J Clin Invest. 2024. https://doi.org/10.1172/JCI173858.

Research In-Press Preview Inflammation

Graphical abstract

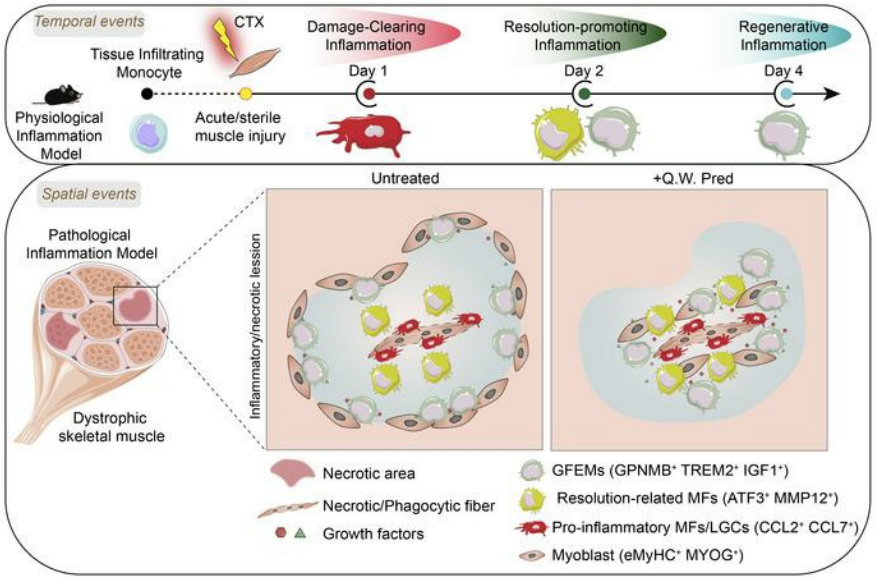

Spatiotemporal transcriptomic mapping of regenerative inflammation in skeletal muscle reveals a dynamic multilayered tissue architecture

Andreas Patsalos[1,#], Laszlo Halasz[1,#], Darby Oleksak[1], Xiaoyan Wei[1], Gergely Nagy[2], Petros Tzerpos[2], Thomas Conrad[3], David W. Hammers [4], H. Lee Sweeney [4], Laszlo Nagy[1,*].

Affiliations

[1]Departments of Medicine and Biological Chemistry, Johns Hopkins University School of Medicine, Institute for Fundamental Biomedical Research, Johns Hopkins All Children's Hospital, St. Petersburg, FL, USA.

[2]Department of Biochemistry and Molecular Biology, Faculty of Medicine, University of Debrecen, Debrecen, Hungary.

[3]Max Delbrück Center for Molecular Medicine, Berlin, Germany.

[4]Myology Institute and Department of Pharmacology and Therapeutics, University of Florida, Gainesville, USA

[#]Equal contribution.

***Corresponding author**: Laszlo Nagy

Address: Johns Hopkins All Children's Hospital, 600 Fifth Street South, St. Petersburg, FL, 33701, USA

Phone: +1-727-767-8928; Email: lnagy@jhmi.edu

Conflict-of-interest statement

The authors have no conflict of interest.

Abstract

Tissue regeneration is orchestrated by macrophages that clear damaged cells and promote regenerative inflammation. How macrophages spatially adapt and diversify their functions to support the architectural requirements of actively regenerating tissue remains unknown. In this study, we reconstructed the dynamic trajectories of myeloid cells isolated from acutely injured and early-stage dystrophic muscles. We identified divergent subsets of monocytes/macrophages and dendritic cells (DCs) and validated markers (e.g., GPNMB) and transcriptional regulators associated with defined functional states. In dystrophic muscle, specialized repair-associated subsets exhibited distinct macrophage diversity and reduced DC heterogeneity. Integrating spatial transcriptomics analyses with immunofluorescence uncovered the ordered distribution of subpopulations and multilayered regenerative inflammation zones (RIZs) where distinct macrophage subsets are organized in functional zones around damaged myofibers supporting all phases of regeneration. Importantly, intermittent glucocorticoid treatment disrupted the RIZs. Our findings suggest that macrophage subtypes mediated the development of the highly ordered architecture of regenerative tissues, unveiling the principles of the structured yet dynamic nature of regenerative inflammation supporting effective tissue repair.

Introduction

Muscle repair following injury involves a well-coordinated immune response, marked by the recruitment of myeloid cells, clearance of damaged tissue, activation of myofibroblasts, and formation of new blood vessels and extracellular matrix (ECM). Central to this process are macrophages (MFs), which regulate satellite cells to restore tissue integrity and function (1) but can also exacerbate disease progression in the context of asynchronous chronic inflammation (2-4). A delicate balance of immune modulation to promote the active resolution of inflammation and expression of growth factors (GFs) is important for emerging muscular dystrophy therapies (5, 6) and underscores the importance of a deep mechanistic understanding of (a) regenerating tissues' histological complexity and (b) the spatiotemporal distribution, kinetics, interactions, and polarization states of innate immune cells in regeneration, a concept termed "*regenerative inflammation*" (1, 7-9).

In response to acute injury, circulating monocytes ($Ly6C^{high}CCR2^{+}CX3CR1^{low}F4/80^{low}$) get activated, extravasate into the injured area, and differentiate into $Ly6C^{low}F4/80^{high}CX3CR1^{high}$ repair MFs (through an *in situ* phenotypic shift) capable of regulating all phases of regeneration (10). A major role of these muscle-infiltrating MFs is the clearance of cellular debris and the secretion of Growth/differentiation factor (GDF)-15, GDF3, insulin-like growth factor-1 (IGF1), other GFs, and ECM proteins to coordinate muscle tissue repair through the regulation of myogenic, fibro/adipogenic, and endothelial cell fates (7, 11-13). Thus, the kinetics of regenerative inflammation are fundamental for the proper orchestration of myogenesis and the coordination of adjacent supportive repair-associated biological processes. Inhibition of the MF maturation/phenotypic shift pathways (including IGF1, MKP1-p38, SRB1-ERK, AMPK, C/EBPβ, STAT3, NFIX, BACH1-HMOX1, PPARγ-RXR-GDF15) prevents the acquisition of the restorative phenotype and impairs regeneration [summarized in (1, 8)]. Premature onset of the repair

phenotype also impairs damage clearing (5, 14-18). Single-cell technologies and trajectory inference analyses now suggest that the monocyte/MF lineage may be more accurately interpreted as a hierarchical continuum of cell states upon tissue injury (19-25). We have identified and characterized four distinct and functional states of repair MFs observed during the repair phase in a myotoxin-induced injury model (7). However, deconvoluting their spatial arrangement and temporal progression through all phases of regeneration, as well as their contribution to tissue organization and function, remains a major challenge.

Here, we combined single-cell and spatially resolved transcriptomics complemented by immunofluorescence (IF) validation to deconvolute the events following muscle injury-induced monocyte infiltration.

Results

Highly ordered distribution of repair MF subtypes during muscle regeneration

We have recently completed a comprehensive immune-specific ($CD45^+$) single-cell transcriptomic (scRNA-seq) analysis of the regeneration phase following acute sterile injury, complementing the wealth of data available (7, 19, 21, 22, 26, 27). Our focused scRNA-seq analyses provide an in-depth annotation of innate immune cell types, subpopulations, and states that dominate the early phases of tissue repair with higher resolution and better-deconvoluted variability than generic non-cell type-specific scRNA-seq approaches, resulting in the identification of four functionally distinct MF subtypes (7). Interestingly, we found that several GFs (i.e., IGF1, GDF3, GDF15) were enriched in a distinct repair MF subpopulation (Growth Factor-Expressing Macrophages; GFEMs). We were able to validate *in vivo* and refine the characterization of this repair MF subset by FACS using a predicted and highly enriched marker (i.e., Glycoprotein Nmb; GPNMB) (7). We reasoned that a spatially resolved view of the regeneration phase is needed to reveal if localization patterns of myeloid subsets exist and are predictive of their function. We used the Spatial Transcriptomics (ST) Visium platform on tibialis anterior (TA) muscles at day 4 post-CTX injury (**Figs. 1A-B** and **S1A**), which is highly dominated by repair-associated MFs (7), to gain insights into their spatial distribution during regeneration.

Two main workflows are used to identify molecular features that correlate with spatial location within a tissue: a) perform differential gene expression (DGE) analysis based on spatially distinct clusters (i.e., pre-annotated pathological/anatomical regions within the tissue based on prior knowledge), and (b) find features that have unique spatial patterning without taking clusters or spatial annotation into account (28). The first strategy using pathologist-annotated areas (see legend for designation criteria) exhibits clear spatial and morphological restriction at the tissue level (**Figs. 1A-B**). The three pathologist-predicted clusters correspond to areas of regenerative

(Cluster 1; C1), inflamed/necrotic (Cluster 2; C2), and healthy (Cluster 3; C3), muscle (**Figs. 1A-B** and **S1B**) and correlate to the expression of relevant functional markers (**Figs. S1C-D**) and GO biological processes (**Fig. S1E**). Interestingly, *Gpnmb* (a marker of GFEMs) is predicted among the top 10 enriched genes in C2 (**Fig. S1D**), indicative of the GFEMs having unique spatial distribution surrounding necrotic areas. To explore the possibility that more detailed spatial co-expression/coherent histological patterns exist, we implemented *BayesSpace* (29), allowing inference of the spatial arrangement of subspots (**Fig. 1C**), enhancing the resolution of gene expression maps (**Figs. 1D** and **S1C**). This resulted in the identification of seven deconvoluted and spatially distinct tissue domains (**Figs. 1C** and **S1F**). GO pathway enrichment analysis corresponding to each resolution-enhanced spatial cluster (**Fig. 1G**) corroborates the existence of more complex histological and functional tissue domains during the regenerative inflammation phase compared to the pathologist annotations seen at spot-level resolution (**Fig. 1A**). The existence of more discrete spatial tissue domains was further supported by the expression pattern of top spatially variable genes (**Fig. 1E**).

Next, we integrated our spatial datasets with a high-resolution immune $CD45^{+}$ scRNA-seq dataset (>7000 single cell profiles; Day 4 post-CTX) (7). This generated a reference to predict the abundance and spatial location of repair MF subsets (7) and other immune cell types in the Visium spots by applying a deconvolution method called *cell2location* (30, 31). Similar to the established benefits of applying non-negative matrix factorization (NMF) to conventional scRNA-seq (32), the additive NMF decomposition generated seven groups of spatial cell type abundance profiles that capture co-localized cell types and subtypes (**Figs. 1F**). The relative abundance and localization of muscle-infiltrating myeloid cells inferred by *BayesSpace* reflected a pattern of coordinated commitment, as shown by antigen-presenting MF subset frequently co-localizing with three DC subsets, while other repair MF subsets have distinct distribution patterns (**Figs. 1G-H**). The spatial

expression patterns of marker genes at subspot resolution for each of these subsets confirm the NMF tissue components prediction (**Fig. S1H**), including GPMNB and GDF15 for GFEMs (MacII; **Figs. 1D, 1I-J,** and **S1H-I**) and CCL7, CCL2, and Ly6C2 for Langhans Giant cells (LGCs appear as a component of MacIII classification; **Figs. 1D, 1H insets,** and **1I**). Interestingly, the MacI (resolution-related MFs) spatial distribution pattern (NMF7) appears to be surrounding areas occupied by LGCs/MacIII and suggests the formation of transcriptionally distinct zones near phagocytosed fibers (**Figs. 1G**-**H** and **S1H**). In summary, the single-cell and ST integration coupled with enhanced subspot resolution clustering assigned the unique cellular distribution of MF and DC subtypes in specific/exclusive multicellular tissue zones during the regenerative inflammation phase.

The sequential and temporal appearance of specialized MF subtypes

Having established the utility of the combination of spatial and single-cell transcriptomics in a single timepoint, we next investigated it as a dynamic time course. Damage-clearing and regenerative inflammation are characterized by the sequential phenotypic transitions of circulating monocytes to pro-inflammatory and then to repair MFs, a process correlated with tissue regeneration kinetics. These reprogramming processes have been documented using several methodologies (5, 18, 33-38), but how the temporal appearance of repair MF subtypes defines the monocytic/MF continuum is unclear.

To understand the MF subtype specification process, we generated an immune cell transcriptomic atlas using droplet-based single-cell 3' RNA-seq (scRNA-seq) in $CD45^{+}$ cells FACS-isolated from CTX-injured TAs at days 1 and 2 and combined datasets from peripheral blood mononuclear cells (PBMCs) and day 4 post-CTX (7) (**Fig. 2A**). We used a compendium of software packages for scRNA-seq data filtering and processing to eliminate dying cells, technical outliers, and doublets (**Fig. S2A**). The resulting *Harmony*-integrated scRNA-seq dataset contained 24,382

cells (**Fig. 2B**). Next, we annotated the major cell types present in this dataset representing the entire immune cell milieu of the regeneration phase following injury (**Fig. 2C**). Identification of cell types was based on the cluster-average expression of canonical genes included in the *ImmGen* Consortium (39) and validated with a nested matrix of per-cell scores (**Fig. S2B**). As expected, the cumulatively largest and most ambiguous group of muscle-infiltrating cells are myeloid-derived, most prominently monocytes and MFs (**Fig. 2C right panel** and **S2C right panel**), classified by the expression of known MF markers like F4/80 (*Adgre1*), and *Trem2* (**Figs. S2C-D**). In addition, DGE in the major cell type clusters provided additional context-dependent markers (**Fig. S2C**). This analysis revealed the dynamics of myeloid cell infiltration and differentiation with early detection of monocytes and a late appearance of DCs (**Fig. 2C right panel**). By focusing on ontogeny-linked populations like monocytes, MFs, and DCs and analyzing them in isolation, we could further discriminate these closely related populations (**Fig. 2D**). By using several frameworks, including sub-sampling cluster robustness metrics and clustering trees to guide the selection of single-cell clustering parameters (40), we were able to initially classify nine distinct clusters, independent of their cell type annotation origin (**Figs. S2E-F** and **S3A-B**). However, considering the annotated cell type origin (**Figs. 2D** and **S3C**) and cluster stability index (**Fig. S2F**) prompted us to manually split cluster 3. The resulting 10 clusters (**Figs. 2E-F**) were then analyzed for unique markers using DGE between cell subpopulations within each cluster and all other cells in the dataset (**Fig. 2G**). Both analyses revealed (a) three subsets of DCs, (b) four different subtypes of monocytes/MFs (including a non-relevant in the context of muscle injury PBMC-originated patrolling Ly6C^{low} monocyte population (37) enriched in cluster 6), and (c) three transitional states (intermediate phenotypes; clusters 2, 5 and 8) with varying cell number composition depending on the timepoint of isolation (**Fig. 2E**) and unique gene expression profiles (**Figs. 2G** and **5A**). We labeled DCs as (a) "Myeloid CD8a^{-}" (cluster 7), (b) "Clec9a^{+}CD8a^{+}" (cluster 9), and (c) "Lymphoid CD8a^{+}"

(cluster 10) (**Figs. 2G** and **5A**) (7). We labeled MFs as "GFEM" (cluster 1), "Resolution-related" (cluster 4), and "Pro-inflammatory" (cluster 3), in agreement with previous findings (7) (**Figs. 2G** and **5A**). We marked the three MF transitional states as "Pro-inflammatory Intermediate" (cluster 2) due to the high-profile similarity to cluster 3, "Antigen-presenting" (cluster 8) due to the high expression of Major Histocompatibility Complex (MHC) genes, and "IFN-regulated" (cluster 5) due to enriched Interferon type I and II signature genes (**Figs. 2G** and **5A**). To uncover the temporal subset dynamics during normal regeneration, we performed pseudotime mapping to infer continuous lineage structures (*Slingshot*; **Fig. 2H**) and RNA velocity (dynamical modeling; scVelo; **Fig. S3D**) underlying differentiation processes (by calculating velocity length; **Fig. S3E**) and detect putative driver genes (**Fig. 2I**). Cluster 3 cells (representing the pro-inflammatory monocytes/MFs) appear first and give rise to four distinct MF and DC lineages. Among the novel and unique markers reported here (**Fig. 2G**), GPNMB (also known as osteoactivin), a marker of the GFEMs (7), is also predicted to be among the drivers of the GFEM lineage (lineage 2; **Figs. 2H-I**). In summary, these findings (a) point towards one single progenitor cell type (infiltrating monocytes) as the origin of all myeloid (MF and DC) subsets accumulating following acute injury and during regeneration and (b) posit a central role for *Gpnmb* expression in the development of GFEMs.

GPNMB is a marker and effector of GFEMs and a regulator of muscle regeneration

In the CTX model, GPNMB expression can accurately predict the presence and abundance of GFEMs when gated for its cell surface expression on $CD45^{+}Ly6C^{low}F4/80^{high}$ repair MFs at day 4 post-CTX (**Fig. S4A**) (7). To evaluate the properties of these cells ($CD45^{+}Ly6C^{low}F4/80^{high}GPNMB^{+}$) and compare them to other repair MF subtypes ($CD45^{+}Ly6C^{low}F4/80^{high}GPNMB^{-}$), we sorted them from WT injured muscle (Day 4 post-CTX) and placed them in culture in equal numbers (**Fig. 3A**). Twelve hours later, we evaluated their survival and activation of apoptosis pathways (assessed by

cleaved Caspase3) (**Figs. 3A-B**). GPNMB^{+} MFs displayed prolonged survival compared to the GPNMB^{-} MFs (**Figs. 3A-B**), indicative of a likely more mature MF subtype (41). To assess paracrine effects, myoblasts were treated with MF supernatant and assayed for proliferation and fusion. GPNMB^{+}Ly6C^{low} MFs supernatant promoted myoblast fusion but had no effect on proliferation, while the GPNMB^{-}Ly6C^{low} MF-derived media had minimal effects in fusion but increased myoblast proliferation (**Figs. 3C-D**). These results support the role of GFEMs (GPNMB^{+}Ly6C^{low}) as the sole repair-associated MF subset secreting GFs and supporting myoblast fusion. Importantly, these GPNMB^{+}CD68^{+} MFs preferentially localize near (<20 µm) regenerating embryonic myosin heavy chain positive (eMyHC^{+}) myofibers compared to other repair-associated MF subsets (CD68^{+}GPNMB^{-}; **Figs. 3E-F**), validating GPNMB as a functional marker of the GFEMs and potentially supporting their crosstalk with other regeneration-associated cells (42).

The DBA/2J strain carries a nonsense mutation in *Gpnmb* (R150X) effectively making these mice a global genetic *Gpnmb* KO (D2.*Gpnmb*$^{-}$) (42-46). Tissue repair following acute injury is severely impaired in this model (42, 47-50), which we confirmed (**Fig. 3G upper panel**). To test the modifying effect of GPNMB on muscle regeneration, we compared CTX-induced muscle repair in D2.*Gpnmb*$^{-}$ and a coisogenic strain with a functional allele of *Gpnmb* (D2.*Gpnmb*$^{+}$) (51). Eight days following CTX injury, we observed a significant increase in centrally nucleated fibers (**Figs. 3G** and **S4B**), regeneration area (**Figs. 3G** and **S4C**), and eMyHC^{+} fibers (**Figs. 3G right panel** and **S4D**), all indicative of a significant improvement in muscle repair, in the D2.*Gpnmb*$^{+}$ mice. Concurrently, D2.*Gpnmb*$^{-}$ CTX-injured muscles exhibited hyperinflammation (increased presence of CD68^{+} MFs) during the late recovery phase of regeneration (day 8 post-CTX), which was significantly reduced/normalized in the D2.*Gpnmb*$^{+}$ mice (**Figs. 3H** and **S4E**). These findings suggest additional autocrine roles of GPNMB in regulating the resolution of inflammation (46). This observation was further supported by (a) quantifying the total number of CD45^{+} muscle-

infiltrating cells, DCs, and neutrophils during the time course of regeneration (**Fig. S4F**), (b) the observed asynchrony in the MF phenotype transition during the regenerative inflammation phase (day 4 post-CTX) using established repair MF maturation markers (**Fig. S4G**) (35), (c) the increased presence of F4/80^{+}CD163^{+} and F4/80^{+}CD206^{+} resolution-related MFs at day 8 post-CTX (**Figs. S4H-I**) and (d) the utilization of ST in regenerating muscles from WT (C57BL/6J) and D2.*Gpnmb*$^{-}$ during the late recovery phase (day 8 post-CTX injury; **Figs. 3I** and **S4J**). While using C57BL/6 mice as controls in this ST experiment has the limitation of inherent differences in inflammatory responses between these two strains (52), its use provides a reference for proper and complete regeneration in a background compatible with the scRNA-seq datasets. Our integrated ST analysis of a total of 2762 spots passing our filtering criteria revealed minimal overlap between samples even after sample batch correction (**Fig. S4K**). Our enhanced clustering analysis at subspot resolution suggests the presence of five spatial clusters (**Figs. 3J** and **S4L**) and revealed major differences in inflammation-and regeneration-related clusters; two of which are overwhelmingly enriched in the D2.*Gpnmb*$^{-}$ samples (clusters 1 and 5; **Fig. 3J**). Predictably, markers of mature MFs (*Adgre1* and *S100a4*) are enriched in the D2.*Gpnmb*$^{-}$ ST samples (**Figs. S4M-N**). Global tissue-wide pseudobulk analysis of differentially expressed genes (DEGs; **Fig. S4N**) and marker analysis of the identified spatial clusters (**Fig. 3K**) revealed that the D2.*Gpnmb*$^{-}$ muscles are characterized by the downregulation of healthy muscle fiber genes (e.g., *Myh4, Pvalb, Actn2, Myh1, Myl1, Ttn*) and overexpression of inflammation-related genes (e.g., *Spp1, Lyz2, Cd68, Mmp9, Mmp12, Lgals3, Ctsk, Fcer1g, S100a4*; **Figs. 3L,** and **S4N**). In addition, the overlap of the spatial expression patterns of *Gpnmb* and *Myh3* in WT regenerating muscle supports our finding that GFEMs preferentially co-localize with regenerating fibers (**Fig. 3M**). Integrating the scRNA-seq dataset from the CTX time course (**Fig. 2F**) to spatially map the different MF and DC subtypes on these muscles using NMF (**Fig. S4O**) revealed that GFEMs' (NMF4) and antigen-presenting subtypes' (including DCs;

NMF3) abundance is markedly reduced in the D2.*Gpnmb*$^{-}$ muscles (**Fig. S4P**). Their distribution is apparent in small regenerating spots compared to the tissue-wide spread distribution seen in normally regenerating WT muscles (**Fig. S4P**). Overall, these results support the unbiased identification of GPNMB as both a marker and an effector of GFEMs.

High-resolution ST view of dystrophic muscle and associated MF subtypes

Given the highly ordered cellular organization of skeletal muscle and the importance of intercellular communication in DMD progression, we reasoned that a spatially resolved view of disease-driven gene expression changes will reveal the relevant myeloid subpopulations and enable comparisons to the ones found in physiological injury/repair. We used a workflow combining ST with the immune-based (CD45^{+}) scRNA-seq approach described above (**Fig. 2A**) to obtain spatial gene expression measurements of D2.*mdx* [a model of Duchenne Muscular Dystrophy (DMD)] (53) skeletal muscle (gastrocnemius; GAST) at a DMD disease stage with seemingly intact regeneration capacity (2 months of age) but still carrying a *Gpnmb* nonsense mutation (**Fig. 4A**). Our ST analysis of 1509 spots passing our filtering criteria revealed a gradient in the detected number of genes per spot (**Fig. S5A**). These differences are consistent between integrated biological replicates (**Figs. S5A-B**) and overlap with pathologist-annotated areas of necrotic/inflammatory lesions, regenerative and healthy tissue (**Fig. 4A**). Enhanced subspot resolution clustering reveals additional spatial domains beyond what the pathologist can annotate based on H&E staining (**Fig. 4A**) for a total of seven spatial clusters (**Figs. 4B** and **S5C**). Marker enrichment analysis for these clusters reveals two distinct inflammatory clusters (clusters 2 and 6), two clusters indicating healthy muscle fibers (clusters 5 and 7), one regenerative (cluster 1), one ECM-related (cluster 4), and one endothelial cell/angiogenesis-related (cluster 3; **Figs. 4C-D**).

The matching scRNA-seq profiles of sorted $CD45^+$ cells (2-mo D2.*mdx*) allowed us to classify seven subsets comprising monocytic, MF, and DC lineages (**Figs. 4E** and **S5D**). These clusters were then analyzed for specific markers using DGE between cells within each cluster and all other cells in the dataset (**Fig. 4F**), resulting in one subset of DC (cluster 5), three different subtypes of MFs (clusters 4, 6 and 7), and two transitional states (intermediate phenotypes; clusters 1, and 2) (**Figs. 4E** and **5B**). To uncover the temporal dynamics in the maturation of these dystrophy-associated subsets, we performed pseudotime mapping by RNA velocity (**Fig. S5E**), assessed the rate of differentiation by calculating velocity length (**Fig. S5F**), and detected putative driver genes (**Fig. S5G**). Integrating the scRNA-seq profiles into the ST dataset predicted six NMF spatial tissue domains where these myeloid subsets localize (**Figs. 4H-I**). This integrative analysis yielded valuable insight into the dystrophic environment regarding the specialized myeloid subpopulations.

Cycling MFs are enriched in dystrophic muscle and present in human DMD

The scRNA-seq analysis and marker prediction of the D2.*mdx* model identified a distinct proliferating MF subset in cluster 6 (**Figs. 4E-G**). These cycling MFs appear as a mature divergent lineage at the end of the pseudotime trajectory, suggestive of a tissue-resident enriched subset (**Fig. S5G**). To confirm the proliferative capacity of these MFs, we bioinformatically mapped the cell cycle stages of each cell in the scRNA-seq dataset (**Fig. 4G**) and then stained acutely injured and dystrophic muscles for Ki67 (**Figs. S5H-J**). We confirmed the enrichment of the cycling MF subset only in the dystrophic muscle (**Figs. S5H-J**). Interestingly, the cycling MF subset is mapped on NMF 3 and 5 along with the DC and infiltrating monocytes, respectively (**Figs. 4H-I**). In contrast, the rest of the myeloid subsets are uniquely assigned to separate NMF domains (**Figs. 4H-I**).

To validate these findings, we re-analyzed publicly available single-nuclei (sn) RNA-seq datasets from vastus lateralis biopsies collected from healthy and DMD patients (**Fig. S3F**) (27). We integrated all samples, batch-corrected the datasets, annotated all cell types, isolated the myeloid subsets (monocyte, MFs, DC) for downstream analysis (**Fig. S3G**), predicted five clusters (**Fig. S3G**) and determined the cell cycle stage of each cell (**Fig. S3H**). Markers such as *PLK1* and *IGF1* confirmed the enrichment of a cycling myeloid subset (cluster 4) and the presence of GFEMs (cluster 3) in human DMD muscles, respectively (**Figs. S3I-J**).

Comparative analysis of myeloid subpopulations in uninjured muscle, physiological regeneration, and dystrophy

We investigated similarities and differences in the myeloid cell type and subtype composition between (a) healthy muscle (tissue-resident) (36), (b) the physiological regeneration-associated, and (c) dystrophy-associated cells (**Fig. 5**). Similarities between acutely injured and dystrophic muscle include MFs being the dominating myeloid cell type in both conditions and the presence of at least one subtype of DCs (**Fig. 5C**). However, the ratio and heterogeneity of the DC populations are substantially reduced in dystrophic muscle; only one predicted monocyte-derived DC subset is observed (**Figs. 5B-D**). A strong correlation regarding gene expression exists between the DMD-enriched cycling (D2.*mdx* cluster 6; **Figs. 4E** and **5B**) and tissue-resident MFs from uninjured muscle (tissue-resident cluster 3; **Fig. 5E**). Concurrently, the GFEMs and resolution-related subtypes converge into a single population with mixed expression profiles and multiple intermediate phenotypes in dystrophic muscles (D2.*mdx* cluster 4; **Figs. 4E, 5B** and **5D-E**). This discrepancy in marker (i.e., *GPNMB* and *IGF1)* expression distribution is also apparent in the human single nuclei DMD datasets (**Figs. S3I-J**). Additional differences can be observed in the magnitude of expression of known regulators and effectors of MF-mediated regeneration (**Fig.**

5F) (7, 12). This suggests that even in the early stages of chronically injured muscles, the subset diversity and compositional dynamics of regenerative inflammation (including the intermediate/transitional phenotypes) are altered.

Damage-clearing and regenerative inflammation form multilayered tissue zones that are sensitive to glucocorticoids

GCs are used to treat DMD to delay loss of ambulation (54). Prolonged daily use, however, has detrimental side effects, including bone demineralization, Cushingoid, cardiomyopathy (55), and muscle atrophy (56, 57). Intermittent dosing has emerged as a potentially less harmful dosing regimen (56). Therefore, the effect of prednisolone (Pred) on RIZ architecture and MF subtype specification was assessed using a 4-week intermittent dosing regimen (5 mg/kg Pred once weekly) in 4-week-old D2.*mdx* mice (**Fig. S6A**). The expression of over 2000 genes per spot was mapped on the Pred-treated GAST muscles using ST (**Figs. 6A-B**), with seven distinct spatial clusters (**Figs. 6B** and **S6C**) and markers (**Fig. S6E**) deconvoluted at subspot resolution. By integrating the ST data from non-treated dystrophic muscles (**Fig. S6D**), we compared the impact of Pred-treatment on spot distribution and cluster composition (**Fig. 6C**). More specifically, we observed increased spatial expression of GC receptor targets (*Tsc22d3, Dusp1, Fkbp5, Per1*), and atrophy-associated genes (*Fbxo32, Gadd45g, Trim63*; **Figs. 6D-E**). These findings suggest that atrogene expression occurs regardless of GC dosing frequency. Additionally, weekly Pred treatment resulted in a significant decrease in the expression of inflammatory (e.g., *Lyz2, Spp1, S100a4, Lgals3, Cd68, Trem2*), ECM (e.g., *Col1a1, Lum, Col3a1, Fn1, Fbn1*), and regenerative genes (e.g., *Igf1, Postn, Myh3, Myog, Myod1, Myl4*; **Figs. 6D-E** and **S6F**). These cluster-specific data are supported by global spot-level pseudobulk gene expression differences (**Fig. 6F;** tissue-wide top DEGs), gene enrichment GO pathway analysis (**Fig. 6G**), and are consistent with prior data (56).

Mapping the MF subtypes isolated from untreated dystrophic muscles (**Fig. 4E**) to the Pred-treated muscle using NMF and *Cell2location's* spatial mapping model also reveals a similar pattern of distribution around necrotic and regenerative areas but a substantial reduction in GFEM/resolution-related cell abundance (**Fig. 6H-I;** cluster 4).

These findings prompted us to inspect the necrotic/inflammatory and regenerating areas in both untreated and Pred-treated dystrophic muscle. A magnified view of these ST areas in untreated dystrophic muscle revealed layered structures and cell distribution (**Fig. 7A**). According to the MF subtype distribution and predicted markers, these zones have (1) pro-inflammatory MFs forming LGCs (58) in the center of lesions around necrotic/phagocytic fibers (Zone A), (2) a layer of resolution-related MFs and GFEMs creating a cell barrier between the inflammatory lesion and the healthy/regenerating areas (Zone B), and (3) newly regenerating fibers occupying the periphery of the lesion, likely receiving the growth signals from the GFEMs (Zone C; **Figs. 7A**). In contrast, in Pred-treated muscles, the outer layer representing the regenerating fibers (Zone C) is absent (**Fig. 7B**). To select specific subspots and quantify these zones and cellular distribution in our ST data, we developed an R *Shiny* application that compares a histologically defined RIZ model to the observed expression of regenerating fibers (e.g., *Myh3, Myog*, *Myl4*) and MF subtype-specific markers (e.g., *Ccl7*, *Ccl2*, *Il1rn*, *Mmp12*, *Nckap1l*, *Itgb2, Atf3*). This quantification validated the expected layered RIZ model in early-stage dystrophic muscle (obs/exp ratio = 0.78; **Fig. 7A**) and the collapse of Zone C with Pred treatment (obs/exp ratio = 0.017; **Fig. 7B**). Global tissue-wide subspot analysis of the RIZs reveals minimal spatial correlation of zone- and cell type-specific markers mapped in degenerative and regenerative foci of untreated muscles (**Fig. 7C left panel**), suggesting RIZs having distinct spatial architecture. This negligible spatial expression overlap could be further recapitulated by individual inspection of additional ST-predicted RIZ-specific markers (*Ccl2, Il1rn, Nckap1l, Itgb2, Myl4, Myog*; **Figs. 7C-D**). Importantly, a significantly higher pairwise

spatial correlation between zone-specific markers in Pred-treated muscles was evident, indicating the loss of the expected spatial distinction of these structures (**Fig. 7C right panel**). Next, we validated the existence and spatial architecture of the RIZs in adult 2-mo D2.*mdx* untreated muscle (**Figs. 7E** and **S7A**) and the effect of Pred treatment (**Figs. 7G** and **S7C**) by IF and calculated the cell densities and average distances extending up to 500 μm from the boundary of a given necrotic lesion (**Figs. 7F, S6G,** and **S7B**). Furthermore, we expanded the panel of antibodies to include other ST-predicted MF subtype markers that can be used to detect RIZs in dystrophic lesions (**Fig. S7D**). Overall, these data demonstrate that Pred treatment diminishes the muscle's capacity to regenerate extensive lesions and causes the disorganization of zone-specific markers (**Figs. 7G, S6G,** and **S7C**), in agreement with the ST (**Fig. 7B-C**). These findings suggest that GCs destabilize RIZs (overlap of Zones A/B and loss of Zone C), which may be the tissue architectural cause of hindered regeneration.

To confirm the presence of RIZs on an independent dataset, we re-analyzed available ST datasets from early-stage dystrophic muscles (59, 60) using our enhanced subspot resolution and clustering *BayesSpace* workflow. Our ST analysis of mouse GAST tissue from young 6-week-old D2.*mdx* untreated animals validated the presence of RIZs and provided additional insights into the molecular landscape of dystrophic muscle (**Fig. S8**). More specifically, histological examination delineated distinct zones of tissue pathology (**Fig. S8A**), as described previously in our 2-mo D2.*mdx* ST samples (**Fig. 4A**), while advanced subspot resolution clustering identified an equal number of seven spatial clusters correlating with various states of muscle inflammation and structured regeneration (**Fig. S8B**). Gene expression profiling within these clusters validated the clustering and suggested cellular activity: *Pvalb* marked the quiescent state of healthy muscle in cluster 7, while *Csf1, Ly6c2,* and *Ccl7* were characteristic of neutrophils and monocyte derived-LGCs within cluster 2, indicative of a specialized pro-inflammatory/phagocytic response. *Mmp12,*

Atf3, and *Nckap1l* expression identified GFEMs and mature MFs engaged in tissue resolution within cluster 6, and *Myh8* and *Myl4* marked the emergence of regenerating muscle fibers in cluster 1 (**Fig. S8C**). A closer examination of specific lesions revealed that the RIZ organization and architecture (**Fig. S8D**) were consistent with spatial patterns previously characterized in our study (**Figs. 7A, 7C-E, S7A-B**). Interestingly, analysis of prominent inflamed regions in these younger (6-week-old) animal samples unveiled unique spatial clustering indicative of a recent injury, with an absence of clusters representing the advanced regeneration stages and a predominance of phagocytes and necrotic fibers (**Fig. S8E**). These findings suggest an ongoing response to recently inflicted focal damage, which is observed by the increase in marker-specific IF signal intensity in these regions (**Fig. S7E**). Overall, these findings provide additional support for the existence of MF-organized RIZs, which are responsive to pharmacological interventions.

The GFEM transcriptional program depends on ATF3

Lastly, we sought to identify the potential transcription factor(s) (TFs) driving the gene networks of GFEMs. *De novo* motif analysis using accessible chromatin regions revealed distinct motif matrices (i.e., PU-box, TRE, M-box, C/EBP) with expected (i.e., PU.1, JUN, FOS; lineage determining factors) (18), and unexpected (i.e., ATF3, and USF2) TF binding enrichment around transcription start sites (TSSs) of GFEM-linked markers (**Fig. 8A**). While *Gpnmb* is a documented target of MITF/TFE across various cell types, including myeloid cells (61-63), close examination by capture Hi-C and predictive modeling of TF interaction with distal and proximal regulatory elements of the *Gpnmb* locus suggests Activating transcription factor 3 (ATF3) playing a central role in its regulation (**Figs. 8B-C**). This was evidenced by enriched motif scores (**Fig. 8B**), clear demarcation of ATF3 and its cofactor JUN binding at muscle MF-specific chromatin accessible sites (**Fig. 8C**) and consistent alignment of ATF3 binding with other markers of transcriptional activity,

including active histone modification (H3K27Ac) and elongating RNA polymerase II (**Fig. 8C**). Notably, the regulatory domain architecture defined by two chromatin structure regulators, namely the genome-wide insulator CTCF and the cohesin ring subunit RAD21, coincided with the positioning of strong ATF3 binding sites (**Fig. 8C**). In parallel, the transcriptional landscape of myeloid cell subtypes depicted in the CTX-based scRNA-seq dataset substantiated our prediction by the unbiased inclusion of ATF3 in the highest tier of expressed TFs (**Fig. 8D**). ATF3's spatial gene (**Figs. 8E-F, 7C,** and **S8D-E**) and protein (**Figs. 8G** and **S7F**) expression patterns in D2.*mdx* muscle suggests a targeted response within RIZs (surrounding LGCs and overlapping with resolution-related MFs). Furthermore, comparative mRNA expression analysis in WT and *Atf3*$^{-/-}$ bone marrow-derived macrophages (BMDMs) (a) underscores ATF3's direct influence on basal GFEM-like marker gene regulation (**Fig. 8H**), and (b) bolsters ATF3's central regulatory role in *Gpnmb* expression (**Fig. 8I**). These findings align with reports on ATF3's regulatory functions within innate immune cells (64-68). Overall, in our extensive epigenomic investigation of primary MFs, integrating Capture Hi-C, ATAC-seq, and ChIP-seq, we identified the TF ATF3 as a direct regulator of a gene expression module resembling that of a GFEM-like transcriptional network.

Discussion

The spatiotemporal ordering of molecular events that drive regenerative inflammation and MF subtype specification in physiological repair and dystrophy remains unclear. Inherent limitations of current gene expression profiling technologies, such as low throughput or lack of spatial context, impede the understanding of how different subtypes interact in space to coordinate regeneration and, importantly, how immune asynchrony affects DMD progression. In this study, (a) we carried out a comprehensive high-dimensional transcriptomic analysis of MF subpopulations in acute and chronic injury models, (b) mapped the spatial distribution of the MF subsets, (c) validated a predicted GFEM marker (GPNMB) and its impact in regeneration, (d) identified ATF3 as a key TF in *Gpnmb* expression and GFEM regulation, (e) discovered a disease-associated subset that is enriched and present in human DMD pathology, and (f) evaluated the impact of intermittent GC treatment on the newly identified multilayered RIZs. Our computational analyses increased ST resolution and, by estimating myeloid subtype compositions at each location, linked the organization of injured and regenerating muscle at different time points to various histomorphological regions of the complex dystrophic muscle.

Recent studies have presented transcriptomic atlases of regenerating and dystrophic muscle, especially highlighting parenchymal and progenitor cells (19, 22, 26, 27, 69-71). Here, we present the analyses of comprehensive immune-specific single-cell and ST datasets of regenerating muscle post-acute injury and during dystrophy, providing deep spatial annotation of myeloid subpopulations with enhanced subspot resolution. This approach enables us to understand changes in monocytic/MF/DC states based on spatial distribution/proximity and their transcriptional and regulatory variations. Additionally, our scRNA-seq analysis offers a trajectory perspective on myeloid cell types, highlighting early monocyte infiltration as the main source of progenitors. The lack of proliferative signatures in CTX injury-related MFs and negligible naive

monocyte profiles beyond the acute injury phase indicate their limited role in later reparative stages. Moreover, the fact that the expression of early monocyte markers like *Vcan* is limited to the first two days post-injury is consistent with the temporally restricted nature of monocyte infiltration. While the trajectories of MF markers *Aif1*, *Adgre1*, and *Csf1r* (72) align with early MF activation stages, they do not maintain peak expression at the end of differentiation. This suggests an earlier role for CSF1 signaling in MF subtype specification and supports a model where reparative MFs derive from early-infiltrating monocytes rather than continuous monocyte infiltration throughout regeneration.

Analysis of the scRNA-seq timecourse identified different states and subtypes of myeloid cells, including ones associated with spatial distribution and disease conditions. Leveraging our integrated data, we inferred and identified potential regulators of MF subtypes. The identification of GPNMB as a GFEM marker (7) and effector of regeneration has important ramifications for the D2.*mdx* DMD model (53). In other models of acute injury, $GPNMB^{+}CD68^{+}$ MFs are also found during the recovery phase and have been suggested to regulate the balance between fibrosis and fibrolysis (47), possibly contributing to the accelerated fibrotic DMD disease progression observed in the D2.*mdx* model. In parallel, unresolved inflammatory gene expression and the prolonged presence of anti-inflammatory $CD206^{+}$ and $CD163^{+}$ MFs with increased antigen-presenting capacity in the absence of functional GPNMB is in line with an additional autocrine role of GPNMB in regulating the resolution of sterile inflammation and pointing towards a protective role in muscle injury by modulating the polarization of MFs (42, 46, 49, 73, 74). Interestingly, the cleaved ectodomain of GPNMB may also act as a paracrine GF, influencing the behavior of nearby cells and participating in the complex interplay of signaling required for regeneration (42, 75-78). Future studies should aim to delineate the specific, context-dependent functional contributions of both the membrane-bound and soluble forms of GPNMB.

In the context of dystrophy, the identification of an enriched mature cycling MF subset is intriguing. The predicted regulators of this subset that involve ECM-depositing genes suggest a *bona fide* fibrotic subset that will establish the later stages of DMD disease progression. A more likely scenario supported by the profile comparison with tissue-resident MFs in uninjured muscle (36) indicates the enrichment of a muscle-resident locally proliferating subset that expands to sufficient numbers to uniquely cluster. This is probably dependent on the disease stage at the time of muscle isolation, and thus, longitudinal studies are warranted to validate this observation. A well-conserved mature MF subset was also found between acutely (cluster 5) and chronically injured (cluster 7) muscles with strong Interferon type I signatures and could reflect the enrichment of muscle-resident MFs (36). The exact function of this subset is not clear, but they may be similar to the function of regenerative bystander DCs that confer protection from subsequent infections (79). Lastly, our findings stemming from the comparison of the CTX-injury and D2.*mdx*-specific subsets highlight how the preexisting inflammatory environment within dystrophic tissues gradually alters regenerative inflammation and, ultimately, the quality of regeneration.

Interestingly, our ST data reveal a distinct niche demarking the zone surrounding the injured fibers with a border that doesn't appear random between injured, regenerating, and uninjured tissue, marked by *Atf3*, *Mmp12*, *Pla2g7*, *Itgb2*, *Lilrb4*, *Hvcn1*, and *Nckap1l* expression, among others (spatial cluster 6; **Figs. 4C, 7A-D, S7** and **S8**). These markers of Zone B are indicative of several MF-driven mechanisms that act simultaneously to guide zone formation. For example, we have previously shown that lipid mediator changes support MF subtype transitions during muscle regeneration (5). The phospholipase A2 group VII (PLA2G7) is secreted by MFs, can degrade platelet-activating factor, and generate lysophosphatidylcholine to resolve inflammation by modulating MF polarization (80, 81). Increased metalloprotease-12 (MMP12) and leukocyte

immunoglobulin-like receptor B4 (LILRB4) are shown to function as an immune checkpoint and regulate/limit MF activation, differentiation, and polarization during pathogenesis (82).

The formation of the multilayered zones is possibly directed by cell polarity, which is necessary for leukocytes to mediate inflammation and immune responses (83). In tissue injury, migrating cells generate distinct actin assemblies at the front and the back to maintain the physical separation of inflammatory signals. This coordinated control of asymmetric morphology and regulatory signals represents an important form of cell polarity. Cells can polarize directionally in response to subtle spatial cues (e.g., gradients of extracellular chemoattractants) (84). This self-organizing process is mediated by localized scaffolded protein complexes of regulatory proteins such as the NCK-Associated Protein 1 Like (NCKAP1L), predicted in Zone B, to help confine the damage-clearing zone from the regenerative zone (85). It's possible that NCKAP1L and other predicted proteins, such as Hydrogen Voltage-Gated Channel 1 (HVCN1), are required for MF cell polarity and chemotaxis for the proper formation of the multilayered RIZs. In parallel, MFs undergo plasma membrane fusion to form multinucleated cells such as the LGCs, typically found during active inflammatory processes (86). In inflamed muscle, LGCs have been shown to preferentially express CCL7 (58) and we found CCL7 to mark the damage-clearing inflammation zone (Zone A). How multinucleation per se contributes to the functional specialization of mature mononuclear MFs remains unclear. It's possible that cell-cell fusion and multinucleation function to confer LGC-specific activity.

Our findings have important ramifications for DMD therapeutic development, as current approaches seek to replace dystrophin with truncated micro-dystrophins (87). While protective of the muscle, these strategies will likely require small molecule adjuncts to address pre-existing pathology, cardiotoxicity, and immune activation (88, 89). Additionally, the *de novo* expression of dystrophin-based therapies might not benefit advanced-stage DMD patients where the muscle is

already replaced by connective tissue. Tailoring immune-modulating treatments that promote muscle regeneration and resolve unwanted inflammation is one strategy that may overcome some of these issues. Findings of this work include the discovery of distinct damage-clearing and RIZs in early-stage dystrophic muscle resembling the temporal and synchronous MF subtype specification of physiological repair. Interestingly, the RIZs are sensitive even to intermittent GCs. By employing advanced imaging and high-dimensional data analysis, RIZs can be identified and quantified in the context of DMD anti-inflammatory therapies (90-92). Overall, the identification of these dynamic and targetable structures provides opportunities to evaluate disease and impaired regeneration states, assess current therapeutic approaches, and develop strategies to enhance RIZs and associated cell types to preserve these highly ordered architectural foci of regeneration in DMD and likely in other tissues and in other chronic inflammatory diseases.

Methods

Sex as a biological variable

We exclusively examined male mice because DMD is an X-linked disease.

Statistics

ANOVA with Bonferroni correction for multiple testing was used to determine statistical significance. Adjusted *p*-values are stated within figure legends. All experiments were performed using at least three independent experiments from each sample group. For FACS, at least four independent samples were analyzed, and at least $5x10^5$ cells were counted for each population. For histology, at least ten samples were used. In bar graphs, individual data points are shown, and the error bars represent the standard deviation (SD). Student's *t*-tests and ANOVA analyses were performed in GraphPad Prism 10 with 95% confidence intervals, and $p<0.05$ was considered statistically significant.

Study approval

All animal experiments were carried out in accordance with ethical regulations and approved by the IACUCs at Johns Hopkins University (license no: MO21C391) and the University of Florida (protocol #202011094).

Data availability

The Day 4 post-CTX injury scRNA-seq dataset is available in GEO (GSE161467). Day 1 and Day 2 post-CTX injury, D2.*mdx* scRNA-seq data, and Visium ST datasets are under GSE223813. Mouse PBMCs are from the 10X Genomics repository (SC3_v3_NextGem_DI_CellPlex_Mouse_PBMC_10K_Multiplex). Human vastus lateralis snRNA-

seq data are under BioProject PRJNA772047. ATF3 KO BMDM gene expression microarray data are from GSE44034. TF ChIP-seq data include cFOS (SRR2353461, SRR2353465, GSM1875488, GSM1875492), NFE2L2 (SRR3714085, GSM2212311), MAFB (SRR2976081, GSM1964739), PU.1 (SRR3407110), CEBPa (SRR4302495), IRF8 (SRR4302496), RUNX1 (SRR4302498), cJUN (SRR6660224, SRR6660225, GSM2974662, GSM2974663), USF2 (SRR6660274, GSM2974712), ATF3 (SRR10486877, GSM4174754), RXR (SRR25923453), CTCF (SRR1514109, GSM2867715), RAD21 (SRR5937719, GSM3164905), Poll2pS2 (SRR6247019, GSM2845631), H3K27Ac (GSE262945). ATAC-seq data are under GSE129393 and GSE262945. cHi-C data are in GSM7846472. Values for all data points in graphs are reported in the Supporting Data Values file.

Extended Material and Methods

Reagents, assays, protocols, and bioinformatic analysis workflows are detailed in the Supplemental Methods.

Author contributions: A.P., D.O., X.W., P.T., and D.W.H. conducted the experiments. A.P. and L.H. designed the figures. A.P., L.H., and G.N. performed the computational analyses. A.P. and L.N. planned the project, T.C., D.W.H., and H.L.S. provided resources and histological samples, and L.N. supervised the work. A.P. and L.N. drafted, and A.P., D.W.H., and L.N. revised the manuscript. All authors discussed the results and commented on the manuscript.

Acknowledgments: The authors acknowledge the excellent technical assistance of Sarah Nathalie Vitcetz, Diana Skapura, Rebecca Buete, and Dr. Jose Luis Herrera. We also thank Drs. Ignacio Gonzalez-Gomez and Hector Monforte for histological annotations, Dr. Christopher Cherry for bioinformatics assistance, and members of the Nagy laboratory for discussions. This work was supported by: JHACF/ACRI Fellowship (#90105887) and MDA Development Grant (#1064247) to A.P.; OTKA (KKP129909 and FK146945) to G.N.; NIH/NIDDK (R01-DK115924, R01-DK124782) and NIH/NHLBI (R01-HL170426) to L.N.; NIH/NIAMS (R01-AR075637 to H.L.S.; R01-AR083108 to D.W.H.; P50-AR052646 to H.L.S. and D.W.H.). Sequencing was performed at the Max-Delbrueck-Center for Molecular Medicine Centre and supported by the EASI-Genomics under EU grant agreement No 824110.

References

1. Patsalos A, et al. Myeloid cell diversification during regenerative inflammation: Lessons from skeletal muscle. *Semin Cell Dev Biol.* 2021;119:89-100.

2. Juban G, et al. AMPK Activation Regulates LTBP4-Dependent TGF-beta1 Secretion by Pro-inflammatory Macrophages and Controls Fibrosis in Duchenne Muscular Dystrophy. *Cell Rep.* 2018;25(8):2163-76 e6.

3. Theret M, et al. Macrophages in Skeletal Muscle Dystrophies, An Entangled Partner. *J Neuromuscul Dis.* 2022;9(1):1-23.

4. Villalta SA, et al. Shifts in macrophage phenotypes and macrophage competition for arginine metabolism affect the severity of muscle pathology in muscular dystrophy. *Hum Mol Genet.* 2009;18(3):482-96.

5. Giannakis N, et al. Dynamic changes to lipid mediators support transitions among macrophage subtypes during muscle regeneration. *Nat Immunol.* 2019;20(5):626-36.

6. Markworth JF, et al. Resolvin D1 supports skeletal myofiber regeneration via actions on myeloid and muscle stem cells. *JCI Insight.* 2020;5(18).

7. Patsalos A, et al. A growth factor-expressing macrophage subpopulation orchestrates regenerative inflammation via GDF-15. *J Exp Med.* 2022;219(1).

8. Caballero-Sanchez N, et al. Regenerative inflammation: When immune cells help to re-build tissues. *FEBS J.* 2022.

9. Karin M, and Clevers H. Reparative inflammation takes charge of tissue regeneration. *Nature.* 2016;529(7586):307-15.

10. Chazaud B. Inflammation and Skeletal Muscle Regeneration: Leave It to the Macrophages! *Trends Immunol.* 2020;41(6):481-92.

11. Joe AW, et al. Muscle injury activates resident fibro/adipogenic progenitors that facilitate myogenesis. *Nat Cell Biol.* 2010;12(2):153-63.

12. Varga T, et al. Macrophage PPARγ, a Lipid Activated Transcription Factor Controls the Growth Factor GDF3 and Skeletal Muscle Regeneration. *Immunity.* 2016;45(5):1038-51.

13. Wosczyna MN, and Rando TA. A Muscle Stem Cell Support Group: Coordinated Cellular Responses in Muscle Regeneration. *Dev Cell.* 2018;46(2):135-43.

14. Bencze M, et al. Proinflammatory macrophages enhance the regenerative capacity of human myoblasts by modifying their kinetics of proliferation and differentiation. *Mol Ther.* 2012;20(11):2168-79.

15. Cheng M, et al. Endogenous interferon-gamma is required for efficient skeletal muscle regeneration. *Am J Physiol Cell Physiol.* 2008;294(5):C1183-91.

16. Perdiguero E, et al. p38/MKP-1-regulated AKT coordinates macrophage transitions and resolution of inflammation during tissue repair. *J Cell Biol.* 2011;195(2):307-22.

17. Rigamonti E, et al. Requirement of inducible nitric oxide synthase for skeletal muscle regeneration after acute damage. *J Immunol.* 2013;190(4):1767-77.

18. Patsalos A, et al. The BACH1-HMOX1 Regulatory Axis Is Indispensable for Proper Macrophage Subtype Specification and Skeletal Muscle Regeneration. *J Immunol.* 2019;203(6):1532-47.

19. De Micheli AJ, et al. Single-Cell Analysis of the Muscle Stem Cell Hierarchy Identifies Heterotypic Communication Signals Involved in Skeletal Muscle Regeneration. *Cell Rep.* 2020;30(10):3583-95 e5.

20. Giordani L, et al. High-Dimensional Single-Cell Cartography Reveals Novel Skeletal Muscle-Resident Cell Populations. *Mol Cell.* 2019;74(3):609-21 e6.

21. McKellar DW, et al. Large-scale integration of single-cell transcriptomic data captures transitional progenitor states in mouse skeletal muscle regeneration. *Commun Biol.* 2021;4(1):1280.

22. Dell'Orso S, et al. Single cell analysis of adult mouse skeletal muscle stem cells in homeostatic and regenerative conditions. *Development.* 2019;146(12).

23. Hwang B, et al. Single-cell RNA sequencing technologies and bioinformatics pipelines. *Exp Mol Med.* 2018;50(8):1-14.

24. Wagner A, et al. Revealing the vectors of cellular identity with single-cell genomics. *Nat Biotechnol.* 2016;34(11):1145-60.

25. Bergen V, et al. RNA velocity-current challenges and future perspectives. *Mol Syst Biol.* 2021;17(8):e10282.

26. Oprescu SN, et al. Temporal Dynamics and Heterogeneity of Cell Populations during Skeletal Muscle Regeneration. *iScience.* 2020;23(4):100993.

27. Scripture-Adams DD, et al. Single nuclei transcriptomics of muscle reveals intra-muscular cell dynamics linked to dystrophin loss and rescue. *Commun Biol.* 2022;5(1):989.

28. Dries R, et al. Advances in spatial transcriptomic data analysis. *Genome Res.* 2021;31(10):1706-18.

29. Zhao E, et al. Spatial transcriptomics at subspot resolution with BayesSpace. *Nat Biotechnol.* 2021;39(11):1375-84.

30. Li H, et al. A comprehensive benchmarking with practical guidelines for cellular deconvolution of spatial transcriptomics. *Nat Commun.* 2023;14(1):1548.

31. Kleshchevnikov V, et al. Cell2location maps fine-grained cell types in spatial transcriptomics. *Nat Biotechnol.* 2022;40(5):661-71.

32. Johnson JAI, et al. Inferring cellular and molecular processes in single-cell data with non-negative matrix factorization using Python, R and GenePattern Notebook implementations of CoGAPS. *Nat Protoc.* 2023;18(12):3690-731.

33. Mounier R, et al. AMPKalpha1 regulates macrophage skewing at the time of resolution of inflammation during skeletal muscle regeneration. *Cell Metab.* 2013;18(2):251-64.

34. Wang H, et al. Altered Macrophage Phenotype Transition Impairs Skeletal Muscle Regeneration. *The American Journal of Pathology.* 2014;184(4):1167-84.

35. Panduro M, et al. Treg cells limit IFN-gamma production to control macrophage accrual and phenotype during skeletal muscle regeneration. *Proc Natl Acad Sci U S A.* 2018;115(11):E2585-E93.

36. Wang X, et al. Heterogeneous origins and functions of mouse skeletal muscle-resident macrophages. *Proc Natl Acad Sci U S A.* 2020;117(34):20729-40.

37. Varga T, et al. Tissue LyC6- macrophages are generated in the absence of circulating LyC6-monocytes and Nur77 in a model of muscle regeneration. *J Immunol.* 2013;191(11):5695-701.

38. Varga T, et al. Highly Dynamic Transcriptional Signature of Distinct Macrophage Subsets during Sterile Inflammation, Resolution, and Tissue Repair. *J Immunol.* 2016;196(11):4771-82.

39. Heng TS, et al. The Immunological Genome Project: networks of gene expression in immune cells. *Nat Immunol.* 2008;9(10):1091-4.

40. Patterson-Cross RB, et al. Selecting single cell clustering parameter values using subsampling-based robustness metrics. *BMC Bioinformatics.* 2021;22(1):39.

41. Mass E, et al. Tissue-specific macrophages: how they develop and choreograph tissue biology. *Nat Rev Immunol.* 2023;23(9):563-79.

42. Yu B, et al. Glycoprotein Nonmelanoma Clone B Regulates the Crosstalk between Macrophages and Mesenchymal Stem Cells toward Wound Repair. *J Invest Dermatol.* 2018;138(1):219-27.

43. Robinet P, et al. Quantitative trait locus mapping identifies the Gpnmb gene as a modifier of mouse macrophage lysosome function. *Sci Rep.* 2021;11(1):10249.

44. Timmermans S, et al. Complete overview of protein-inactivating sequence variations in 36 sequenced mouse inbred strains. *Proc Natl Acad Sci U S A.* 2017;114(34):9158-63.

45. Anderson MG, et al. GpnmbR150X allele must be present in bone marrow derived cells to mediate DBA/2J glaucoma. *BMC Genet.* 2008;9:30.

46. Ripoll VM, et al. Gpnmb is induced in macrophages by IFN-gamma and lipopolysaccharide and acts as a feedback regulator of proinflammatory responses. *J Immunol.* 2007;178(10):6557-66.

47. Kumagai K, et al. Glycoprotein Nonmetastatic Melanoma B (Gpnmb)-Positive Macrophages Contribute to the Balance between Fibrosis and Fibrolysis during the Repair of Acute Liver Injury in Mice. *PLoS One.* 2015;10(11):e0143413.

48. Silva WN, et al. Macrophage-derived GPNMB accelerates skin healing. *Exp Dermatol.* 2018;27(6):630-5.

49. Li B, et al. The melanoma-associated transmembrane glycoprotein Gpnmb controls trafficking of cellular debris for degradation and is essential for tissue repair. *FASEB J.* 2010;24(12):4767-81.

50. Quattrocelli M, et al. Genetic modifiers of muscular dystrophy act on sarcolemmal resealing and recovery from injury. *PLoS Genet.* 2017;13(10):e1007070.

51. Howell GR, et al. Absence of glaucoma in DBA/2J mice homozygous for wild-type versions of Gpnmb and Tyrp1. *BMC Genet.* 2007;8:45.

52. Srivastava B, et al. Host genetic background strongly influences the response to influenza a virus infections. *PLoS One.* 2009;4(3):e4857.

53. Hammers DW, et al. The D2.mdx mouse as a preclinical model of the skeletal muscle pathology associated with Duchenne muscular dystrophy. *Sci Rep.* 2020;10(1):14070.

54. Griggs RC, et al. Efficacy and safety of deflazacort vs prednisone and placebo for Duchenne muscular dystrophy. *Neurology.* 2016;87(20):2123-31.

55. Barp A, et al. Genetic Modifiers of Duchenne Muscular Dystrophy and Dilated Cardiomyopathy. *PLoS One.* 2015;10(10):e0141240.

56. Quattrocelli M, et al. Intermittent glucocorticoid steroid dosing enhances muscle repair without eliciting muscle atrophy. *J Clin Invest.* 2017;127(6):2418-32.

57. Hammers DW, et al. Glucocorticoids counteract hypertrophic effects of myostatin inhibition in dystrophic muscle. *JCI Insight.* 2020;5(1).

58. Chen Y, et al. Insight into the Molecular Characteristics of Langhans Giant Cell by Combination of Laser Capture Microdissection and RNA Sequencing. *J Inflamm Res.* 2022;15:621-34.

59. Stec MJ, et al. A cellular and molecular spatial atlas of dystrophic muscle. *Proc Natl Acad Sci U S A.* 2023;120(29):e2221249120.

60. Coulis G, et al. Single-cell and spatial transcriptomics identify a macrophage population associated with skeletal muscle fibrosis. *Sci Adv.* 2023;9(27):eadd9984.

61. Gutknecht M, et al. The transcription factor MITF is a critical regulator of GPNMB expression in dendritic cells. *Cell Commun Signal.* 2015;13:19.

62. Gabriel TL, et al. Lysosomal stress in obese adipose tissue macrophages contributes to MITF-dependent Gpnmb induction. *Diabetes.* 2014;63(10):3310-23.

63. Ripoll VM, et al. Microphthalmia transcription factor regulates the expression of the novel osteoclast factor GPNMB. *Gene.* 2008;413(1-2):32-41.

64. Labzin LI, et al. ATF3 Is a Key Regulator of Macrophage IFN Responses. *J Immunol.* 2015;195(9):4446-55.

65. Sha H, et al. ATF3 promotes migration and M1/M2 polarization of macrophages by activating tenascin-C via Wnt/beta-catenin pathway. *Mol Med Rep.* 2017;16(3):3641-7.

66. Jadhav K, and Zhang Y. Activating transcription factor 3 in immune response and metabolic regulation. *Liver Res.* 2017;1(2):96-102.

67. Liu S, et al. The Dual Roles of Activating Transcription Factor 3 (ATF3) in Inflammation, Apoptosis, Ferroptosis, and Pathogen Infection Responses. *Int J Mol Sci.* 2024;25(2).

68. De Nardo D, et al. High-density lipoprotein mediates anti-inflammatory reprogramming of macrophages via the transcriptional regulator ATF3. *Nat Immunol.* 2014;15(2):152-60.

69. Kim M, et al. Single-nucleus transcriptomics reveals functional compartmentalization in syncytial skeletal muscle cells. *Nat Commun.* 2020;11(1):6375.

70. Krasniewski LK, et al. Single-cell analysis of skeletal muscle macrophages reveals age-associated functional subpopulations. *Elife.* 2022;11.

71. Rubenstein AB, et al. Single-cell transcriptional profiles in human skeletal muscle. *Sci Rep.* 2020;10(1):229.

72. Hume DA, and MacDonald KP. Therapeutic applications of macrophage colony-stimulating factor-1 (CSF-1) and antagonists of CSF-1 receptor (CSF-1R) signaling. *Blood.* 2012;119(8):1810-20.

73. Saade M, et al. The Role of GPNMB in Inflammation. *Front Immunol.* 2021;12:674739.

74. Zhou L, et al. Glycoprotein non-metastatic melanoma protein b (Gpnmb) is highly expressed in macrophages of acute injured kidney and promotes M2 macrophages polarization. *Cell Immunol.* 2017;316:53-60.

75. Oyewumi MO, et al. Osteoactivin (GPNMB) ectodomain protein promotes growth and invasive behavior of human lung cancer cells. *Oncotarget.* 2016;7(12):13932-44.

76. Furochi H, et al. Osteoactivin fragments produced by ectodomain shedding induce MMP-3 expression via ERK pathway in mouse NIH-3T3 fibroblasts. *FEBS Lett.* 2007;581(30):5743-50.

77. Rose AA, et al. ADAM10 releases a soluble form of the GPNMB/Osteoactivin extracellular domain with angiogenic properties. *PLoS One.* 2010;5(8):e12093.

78. Sondag GR, et al. Osteoactivin inhibition of osteoclastogenesis is mediated through CD44-ERK signaling. *Exp Mol Med.* 2016;48(9):e257.

79. Jin RM, et al. Chronic infection stunts macrophage heterogeneity and disrupts immune-mediated myogenesis. *JCI Insight.* 2018;3(18).

80. Milias GA, et al. Effects of eccentric exercise-induced muscle injury on blood levels of platelet activating factor (PAF) and other inflammatory markers. *Eur J Appl Physiol.* 2005;95(5-6):504-13.

81. Spadaro O, et al. Caloric restriction in humans reveals immunometabolic regulators of health span. *Science.* 2022;375(6581):671-7.

82. Yang T, et al. LILRB4, an immune checkpoint on myeloid cells. *Blood Sci.* 2022;4(2):49-56.

83. Mastrogiovanni M, et al. Cell polarity regulators, multifunctional organizers of lymphocyte activation and function. *Biomed J.* 2022;45(2):299-309.

84. Weiner OD, et al. Hem-1 complexes are essential for Rac activation, actin polymerization, and myosin regulation during neutrophil chemotaxis. *PLoS Biol.* 2006;4(2):e38.

85. Suwankitwat N, et al. The actin-regulatory protein Hem-1 is essential for alveolar macrophage development. *J Exp Med.* 2021;218(4).

86. Ahmadzadeh K, et al. Multinucleated Giant Cells: Current Insights in Phenotype, Biological Activities, and Mechanism of Formation. *Front Cell Dev Biol.* 2022;10:873226.

87. Mendell JR, et al. Assessment of Systemic Delivery of rAAVrh74.MHCK7.micro-dystrophin in Children With Duchenne Muscular Dystrophy: A Nonrandomized Controlled Trial. *JAMA Neurol.* 2020.

88. Emami MR, et al. Innate and adaptive AAV-mediated immune responses in a mouse model of Duchenne muscular dystrophy. *Mol Ther Methods Clin Dev.* 2023;30:90-102.

89. Hart CC, et al. Potential limitations of microdystrophin gene therapy for Duchenne muscular dystrophy. *JCI Insight.* 2024;9(11).

90. Guglieri M, et al. Efficacy and Safety of Vamorolone vs Placebo and Prednisone Among Boys With Duchenne Muscular Dystrophy: A Randomized Clinical Trial. *JAMA Neurol.* 2022;79(10):1005-14.

91. Finkel RS, et al. A Randomized, Double-Blind, Placebo-Controlled, Global Phase 3 Study of Edasalonexent in Pediatric Patients with Duchenne Muscular Dystrophy: Results of the PolarisDMD Trial. *J Neuromuscul Dis.* 2021;8(5):769-84.

92. Del Giudice E, et al. Off-label use of canakinumab in pediatric rheumatology and rare diseases. *Front Med (Lausanne).* 2022;9:998281.

93. Sciorati C, et al. Cell death, clearance and immunity in the skeletal muscle. *Cell Death Differ.* 2016;23(6):927-37.

Figures

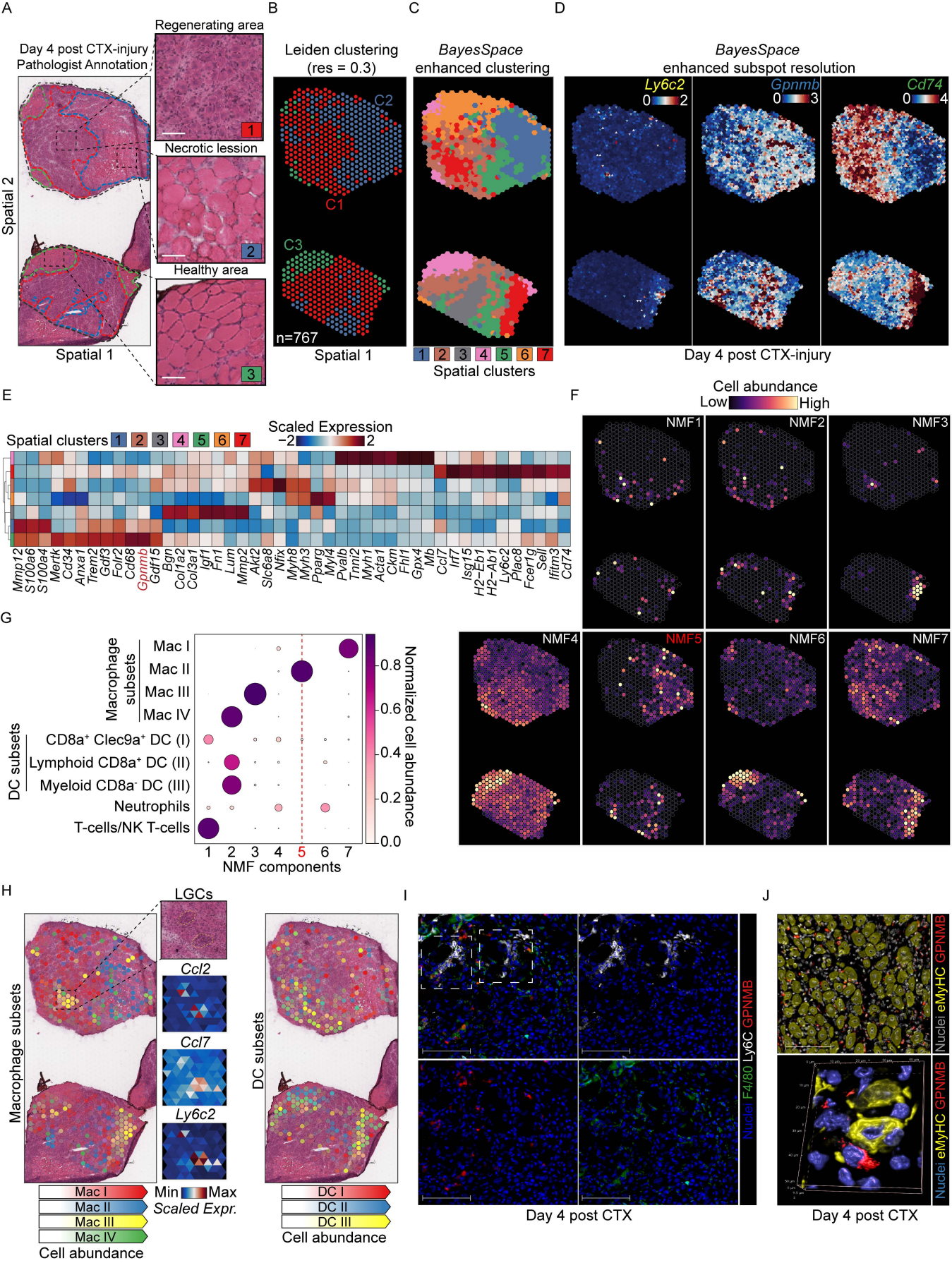
A
Regenerating area
Day 4 post CTX-injury
Pathologist Annotation
Necrotic lesion
Healthy area
Spatial 2
Spatial 1
1
2
3
B
Leiden clustering
(res = 0.3)
C2
C1
C3
n=767
Spatial 1
C
BayesSpace
enhanced clustering
1 2 3 4 5 6 7
Spatial clusters
D
BayesSpace
enhanced subspot resolution
Ly6c2
0 2
Gpnmb
0 3
Cd74
0 4
Day 4 post CTX-injury
E
Spatial clusters 1 2 3 4 5 6 7
Scaled Expression
−2 2
Mmp12
S100a6
S100a4
Mertk
Cd34
Anxa1
Trem2
Gdf3
Folr2
Cd68
Gpnmb
Gdf15
Bgn
Col1a2
Col3a1
Igf1
Fn1
Lum
Mmp2
Akt2
Slc6a8
Nfix
Myh8
Myh3
Pparg
Myl4
Pvalb
Tnni2
Myh1
Acta1
Ckm
Fhl1
Gpx4
Mb
Ccl7
Irf7
Isg15
H2−Eb1
H2−Ab1
Ly6c2
Plac8
Fcer1g
Sell
Ifitm3
Cd74
F
Cell abundance
Low High
NMF1
NMF2
NMF3
NMF4
NMF5
NMF6
NMF7
G
Macrophage subsets
Mac I
Mac II
Mac III
Mac IV
DC subsets
CD8a⁺ Clec9a⁺ DC (I)
Lymphoid CD8a⁺ DC (II)
Myeloid CD8a⁻ DC (III)
Neutrophils
T-cells/NK T-cells
1 2 3 4 5 6 7
NMF components
Normalized cell abundance
0.8
0.6
0.4
0.2
0.0
H
LGCs
Ccl2
Ccl7
Ly6c2
Macrophage subsets
Mac I
Mac II
Mac III
Mac IV
Cell abundance
Min Max
Scaled Expr.
DC subsets
DC I
DC II
DC III
Cell abundance
I
Nuclei F4/80 Ly6C GPNMB
Day 4 post CTX
J
Nuclei eMyHC GPNMB
Nuclei eMyHC GPNMB
Day 4 post CTX

Figure 1. Spatial and single-cell transcriptomics integration and enhanced-resolution clustering resolve the cellular distribution of myeloid subtypes during regenerative inflammation.

A. H&E images of TAs at 4 days post-CTX injury used for ST. Magnified insets indicate histopathological annotations (red-C1: regenerative muscle; blue-C2: necrotic/inflammatory lesions; green-C3: healthy muscle). Area C2 shows segmental necrosis of muscle fibers, including pale fibers with loss of cytoplasmic structures, active phagocytosis, "C" or "Delta" lesions, and membrane damage (93), compared to C1, which includes inflammatory cells and regenerating myocytes. Each section is a different biological replicate. Scale bars: 50 µm.

B. Spatial clustering (Leiden algorithm; cluster resolution 0.3) identifies three discrete regions overlapping with histopathology annotations of **1A**. The number of spots (n=767) is indicated.

C. Enhanced subspot resolution clustering (*BayesSpace*) identified seven spatial domains, not resolved at spot-level clustering.

D. Spatial expression patterns at subspot resolution of genes defining the myeloid subsets characterized by scRNA-seq (7). Color scale shows log-normalized counts for each subspot. Gene label color corresponds to the classification shown in left panel **1H**.

E. Heatmap of the spatial expression of top predicted and curated functional markers, highlighting the specificity of the seven identified spatial *BayesSpace* clusters. *Gpnmb* is highlighted.

F. Identification of tissue compartments using NMF-based decomposition and day 4 post-CTX reference immune subtype expression signatures (7). Spatial plots show cell abundance for each subtype.

G. Dot plot of the estimated NMF weights of cell types/subtypes across seven predicted NMF components. Note the differential abundance of MacII and MacIII subtypes and the overlap of DC subsets with MacIV. MacI: Resolution-related MFs, MacII: GFEMs, MacIII: infiltrating monocytes/pro-inflammatory MFs, MacIV: antigen-presenting MFs (7).

H. Distribution and estimated cell abundance of MF and DC subtypes associated with specific NMF cellular compartments. Insets indicate a histological area on NMF3, predicting MacIII and the formation of LGCs (encircled). The local spatial expression of known markers of LGCs (*Ccl2*, *Ccl7*) (58, 86) overlaps with the histological features and other MacIII markers (*Ly6c2*; **Fig. 1D**, *Plac8*; **Fig. S1E**).

I. IF detection of LGCs (MacIII) and GFEMs (MacII) by GPNMB, Ly6C, and F4/80 (green) in C57BL/6J animals at day 4 post-CTX injury. Split channels are shown. White boxes indicate two LGC-like structures. Scale bars: 100 µm.

J. Upper: IF of $GPNMB^{+}$ MFs and $eMyHC^{+}$ fibers at day 4 post-CTX injury. Lower: High-resolution volume projection confocal image of $GPNMB^{+}$ MFs and $eMyHC^{+}$ regenerating fibers preferential spatial proximity (3D reconstruction distances are indicated). Scale bar: 100 µm.

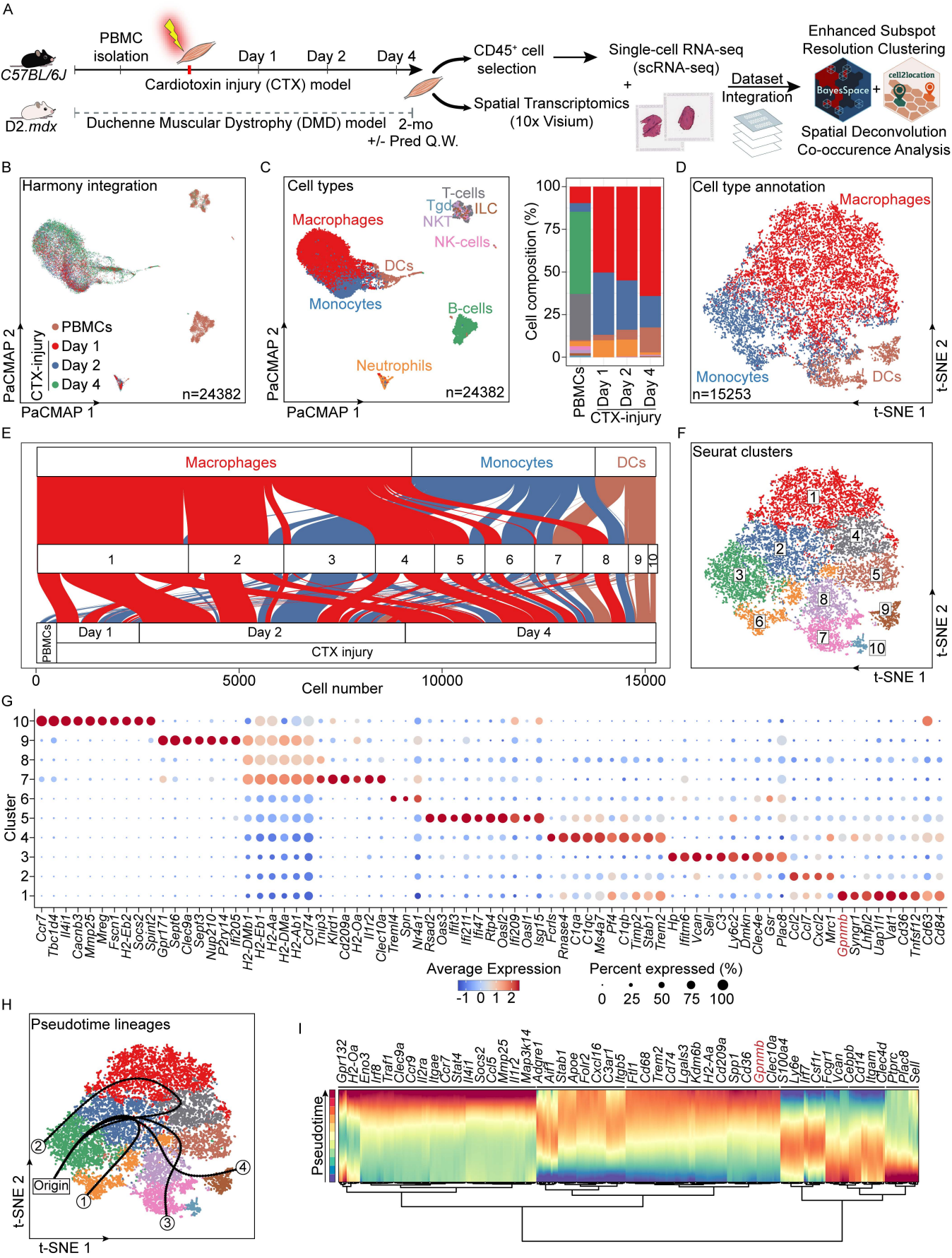
A
C57BL/6J
PBMC isolation
Day 1
Day 2
Day 4
Cardiotoxin injury (CTX) model
D2.mdx
Duchenne Muscular Dystrophy (DMD) model
2-mo +/- Pred Q.W.
CD45+ cell selection
Single-cell RNA-seq (scRNA-seq)
Spatial Transcriptomics (10x Visium)
Dataset Integration
Enhanced Subspot Resolution Clustering
BayesSpace
cell2location
Spatial Deconvolution
Co-occurence Analysis
B
Harmony integration
PBMCs
Day 1
Day 2
Day 4
CTX-injury
n=24382
PaCMAP 1
PaCMAP 2
C
Cell types
T-cells
Tgd
ILC
NKT
Macrophages
NK-cells
DCs
Monocytes
B-cells
Neutrophils
n=24382
Cell composition (%)
D
Cell type annotation
Macrophages
Monocytes
DCs
n=15253
t-SNE 1
t-SNE 2
E
Macrophages
Monocytes
DCs
PBMCs
Day 1
Day 2
Day 4
CTX injury
Cell number
F
Seurat clusters
G
Cluster
Average Expression
Percent expressed (%)
H
Pseudotime lineages
Origin
I
Pseudotime

Figure 2. The sequential appearance of specialized MF subtypes orchestrates skeletal muscle regeneration.

A. Schematic of the analysis workflow for generating immune ($CD45^+$) scRNA-sequencing and ST (Visium) of regenerating and dystrophic muscle. Cell suspensions were collected from digested TAs of adult mice at 1, 2, and 4 days post-CTX injury and steady-state GAST of 2-mo D2.*mdx*. PBMC datasets from non-injured C57BL/6J mice were downloaded from the 10X Genomics repository. Enhanced spatial resolution, deconvolution, and co-occurrence of myeloid subtypes are achieved by single-cell and spatial dataset integration (*BayesSpace* and *Cell2location*).

B. Single-cell transcriptomes from $CD45^+$ cells sorted at days 1, 2, and 4 post-CTX injury, and PBMCs were *harmony*-integrated and batch-effect corrected. Data (24,382 cells) are presented as a PaCMAP projection and color-coded by sample origin.

C. Integrated transcriptomic atlas of 10 major populations (*SingleR* automated cell type annotation using the *ImmGen* database). Cell types are color-colored. Right: Cell-type proportions and compositional dynamics. MFs account for 41.2% of all immune cells.

D. Cells in the macro-clusters of interest (Monocytes, MFs, and DCs) were reanalyzed in isolation. t-SNE visualization reveals local differences. Cells are colored by major cell type classification.

E. Clustering of the isolated cell types from **2D** resolved 10 subtypes of monocytes, MFs, and DCs. Subcluster composition (absolute cell numbers) is presented as an alluvial plot.

F. t-SNE visualization of the 10 subtypes of monocytes, MFs, and DCs.

G. Dot-plot of top DEGs distinguishing the 10 monocyte/MF/DC clusters (three DC; clusters 7, 9 and 10; two monocytic; clusters 3 and 6, two MF subtypes; clusters 1, 4; and three MF transitional states; clusters 2, 5, and 8; **Fig. 5A**). Dot size represents the percentage of

cells expressing each marker within a cluster. *Gpnmb*, the top GFEM marker (cluster 1) is highlighted in red.

H. t-SNE colored by cluster and inferred pseudotime (*Slingshot;* principal curves are smoothed representations of each lineage) with four predicted cell fates: one monocyte (patrolling monocytes), one MF (GFEMs), and two DC lineages. Origin determines the circulating Ly6C^{hi} monocyte population, projected at the start of all trajectories. Trajectory 1 predicts the patrolling monocyte differentiation that is not relevant in the context of injury (37).

I. Gene expression dynamics of the 10 monocyte/MF/DC subpopulations resolved along latent time. Cells were subjected to trajectory inference using *Monocle*'s differential expression analysis to identify lineages. Top likelihood-ranked genes by branch and pseudotime are shown. *Gpnmb* is highlighted.

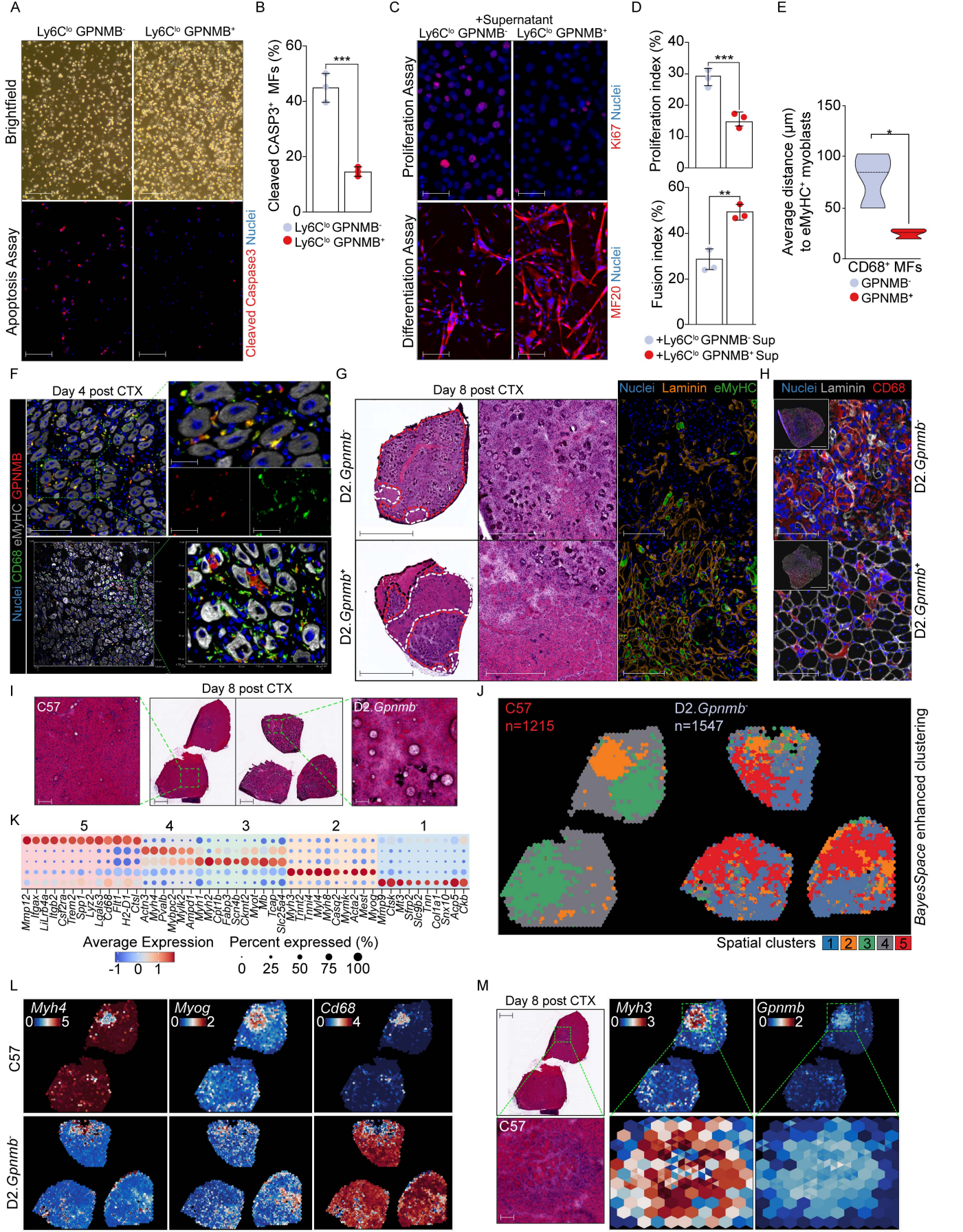
A
Ly6C^lo GPNMB^-
Ly6C^lo GPNMB^+
Brightfield
Apoptosis Assay
Cleaved Caspase3 Nuclei
B
Cleaved CASP3^+ MFs (%)
***
Ly6C^lo GPNMB^-
Ly6C^lo GPNMB^+
C
+Supernatant
Proliferation Assay
Ki67 Nuclei
Differentiation Assay
MF20 Nuclei
D
Proliferation index (%)
***
Fusion index (%)
**
+Ly6C^lo GPNMB^- Sup
+Ly6C^lo GPNMB^+ Sup
E
Average distance (µm) to eMyHC^+ myoblasts
*
CD68^+ MFs
GPNMB^-
GPNMB^+
F
Day 4 post CTX
Nuclei CD68 eMyHC GPNMB
G
Day 8 post CTX
Nuclei Laminin eMyHC
D2.Gpnmb^-
D2.Gpnmb^+
H
Nuclei Laminin CD68
D2.Gpnmb^-
D2.Gpnmb^+
I
Day 8 post CTX
C57
D2.Gpnmb^-
J
C57
n=1215
D2.Gpnmb^-
n=1547
BayesSpace enhanced clustering
Spatial clusters 1 2 3 4 5
K
5 4 3 2 1
Mmp12 Itgax LiLrb4a Itgb2 Csf2ra Trem2 Spp1 Lyz2 Lgals3 Cd68 Fit1 H2-D1 Ctsl Actn3 Myh4 Pfkm Mybph2 Mylk2 Ampd1 Myh1 Myh2 Cpt1b Fabp3 Scn4b Ckmt2 Myot Mb Tcap Slc25a4 Myh3 Tnni2 Tnni4 Myh8 Myh13 Casq1 Mstn Actn2 Mest Myog Mmp9 Ctsk Mt3 Sfrp2 Slc9b2 Tnn Col1a1 Snx10 Acp5 Ckb
Average Expression
-1 0 1
Percent expressed (%)
0 25 50 75 100
L
Myh4
0 5
Myog
0 2
Cd68
0 4
C57
D2.Gpnmb^-
M
Day 8 post CTX
Myh3
0 3
Gpnmb
0 2
C57

Figure 3. GPNMB is a marker and component of GFEMs, and its deficiency impairs regeneration.

A. Upper: Brightfield images of day 4 post-CTX Ly6C^{lo}F4/80^{hi}GPNMB^{-} and Ly6C^{lo}F4/80^{hi}GPNMB^{+} muscle-infiltrating MFs *ex vivo* after 12 hours in culture (equal number of cells were seeded from each sorted population). Lower: Apoptosis was assessed in the same cells by Cleaved Caspase3 immunostaining. Scale bars: 100 µm.

B. Percentage of apoptotic (CASP3+) Ly6C^{low}F4/80^{hi}GPNMB^{+} and Ly6C^{low}F4/80^{hi}GPNMB^{-} MFs (unpaired *t*-test with a p=0.0007; n=3).

C. Effect of GPNMB^{-} and GPNMB^{+} MF-derived conditioned media on the proliferation and differentiation of C2C12 myoblasts. Scale bars: 100 µm.

D. Quantification of the effect of GPNMB^{-} and GPNMB^{+} MF-derived conditioned media on C2C12 myoblasts (n=3). Proliferation index as percentage of Ki67^{+} cells (n=10 fields/group; unpaired *t*-test, p=0.0008). Fusion index as percentage of myotubes (visualized by heavy chain of myosin II) with >3 nuclei (n=10 fields/experiment/group; unpaired *t*-test, p=0.002).

E. Spatial cell proximity quantification of GFEMs (CD68^{+}GPNMB^{+}) vs. other MF subtypes to regenerating eMyHC^{+} fibers at day 4 post-CTX in C57BL/6J animals (n=3; >200 mm^2 tissue area/sample; unpaired *t*-test, p=0.0267).

F. Detection of GFEMs by CD68 and GPNMB, in relation to eMyHC^{+} fibers in C57BL/6J animals at day 4 post-CTX injury. Insets indicate the split channels. Scale bars: 100 µm (left) and 20 µm (insets). Lower panel indicates high-resolution volume projection confocal images (3D reconstruction distances are shown).

G. Left: H&E images of D2.*Gpnmb*$^{-}$ (KO) and D2.*Gpnmb*$^{+}$ (WT) TAs at day 8 post-CTX injury. Note the near complete absence of regenerating fibers (highlighted in white) and extensive inflammation areas (highlighted in red) in the D2.*Gpnmb*$^{-}$. Right: IF detection of

newly formed fibers by eMyHC in D2.*Gpnmb*$^{-}$ and D2.*Gpnmb*$^{+}$ TAs at day 8 post-CTX injury. Scale bars: 1 mm (left H&E) and 500 µm (right H&E); 100 µm (IF panels).

H. IF detection of mature MFs by CD68 in KO and WT at day 8 post-CTX injury, correlating to the extent of unresolved inflammation. Scale bars: 100 µm (main) and 1 mm (insets).

I. H&E images of regenerating TAs (day 8 post-CTX-injury) from WT (C57BL/6J) and D2.*Gpnmb*$^{-}$ animals used for ST. Insets show magnified H&E areas (green rectangles).

J. Enhanced subspot resolution clustering of regenerating TAs (day 8 post-CTX injury) from WT and D2.*Gpnmb*$^{-}$ identified five spatial clusters (n spots/group is indicated).

K. Top marker gene expression after z-score transformation for each spatial cluster. Dot size represents the percentage of subspots expressing the gene.

L. Spatial expression of representative healthy muscle (*Myh4*), differentiating myoblasts (*Myog*), and persistent inflammation/mature MFs (*Cd68*) genes in WT and D2.*Gpnmb*$^{-}$. Note the loss of the distinct structure of regenerative zones in the KO.

M. *Gpnmb* and *Myh3* spatial expression patterns in the C57BL/6J day 8 post-CTX ST sample confirm the proximity of GPNMB^{+} MFs to early-stage regenerating fibers and distinct tissue organization around lesions. Scale bars: 1 mm (upper) and 100 µm (lower). H&E previously presented in **3I**. This duplication is intended to provide the location and context for the presented magnified feature plots.

In all bar graphs, bars represent mean ± SD (*p<0.05, **p<0.01, ***p<0.001).

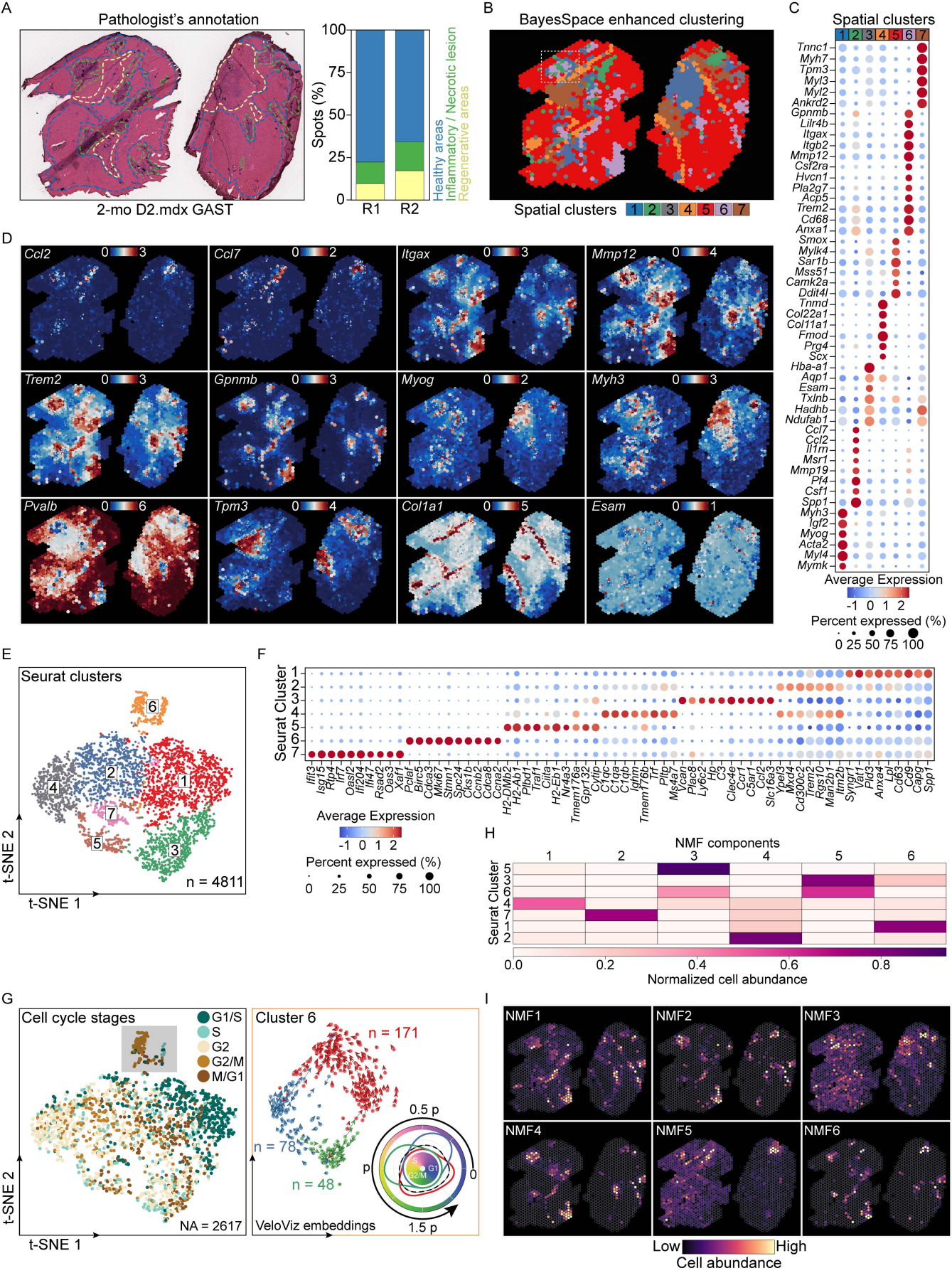
A
Pathologist's annotation
2-mo D2.mdx GAST
Spots (%)
100
75
50
25
0
R1
R2
Healthy areas
Inflammatory / Necrotic lesion
Regenerative areas
B
BayesSpace enhanced clustering
Spatial clusters
1 2 3 4 5 6 7
C
Spatial clusters
1 2 3 4 5 6 7
Tnnc1
Myh7
Tpm3
Myl3
Myl2
Ankrd2
Gpnmb
Lilr4b
Itgax
Itgb2
Mmp12
Csf2ra
Hvcn1
Pla2g7
Acp5
Trem2
Cd68
Anxa1
Smox
Mylk4
Sar1b
Mss51
Camk2a
Ddit4l
Tnmd
Col22a1
Col11a1
Fmod
Prg4
Scx
Hba-a1
Aqp1
Esam
Txlnb
Hadhb
Ndufab1
Ccl7
Ccl2
Il1rn
Msr1
Mmp19
Pf4
Csf1
Spp1
Myh3
Igf2
Myog
Acta2
Myl4
Mymk
Average Expression
-1 0 1 2
Percent expressed (%)
0 25 50 75 100
D
Ccl2 0 3
Ccl7 0 2
Itgax 0 3
Mmp12 0 4
Trem2 0 3
Gpnmb 0 3
Myog 0 2
Myh3 0 3
Pvalb 0 6
Tpm3 0 4
Col1a1 0 5
Esam 0 1
E
Seurat clusters
1
2
3
4
5
6
7
t-SNE 2
t-SNE 1
n = 4811
F
Seurat Cluster
1
2
3
4
5
6
7
Ifit3
Isg15
Rtp4
Ifit7
Oasl2
Ifi204
Ifi47
Rsad2
Oas3
Xaf1
Pclaf
Birc5
Cdca3
Mki67
Stmn1
Spc24
Cks1b
Ccnb2
Cdca8
Cenpa
H2-Ab1
H2-Aa
Pilrb1
Traf1
Cilp
H2-Eb1
Nr4a3
Tmem176a
Gpr132
Cytip
C1qc
C1qa
C1qb
Iglhm
Tmem176b
Trf
Pltp
Ms4a7
Vcan
Plac8
Ly6c2
Hp
C3
Clec4e
Ccr1
C5ar1
Ccl2
Slc16a3
Ypel3
Mxd4
Cd300c2
Trem2
Rgs10
Man2b1
Itm2b
Syngr1
Vat1
Pld3
Anxa4
Lpl
Cd63
Cd9
Capg
Spp1
Average Expression
-1 0 1 2
Percent expressed (%)
0 25 50 75 100
H
NMF components
1 2 3 4 5 6
Seurat Cluster
5
3
6
4
7
1
2
0.0 0.2 0.4 0.6 0.8
Normalized cell abundance
G
Cell cycle stages
G1/S
S
G2
G2/M
M/G1
t-SNE 2
t-SNE 1
NA = 2617
Cluster 6
n = 171
n = 78
n = 48
0.5 p
p
0
1.5 p
S
G1
G2/M
VeloViz embeddings
I
NMF1
NMF2
NMF3
NMF4
NMF5
NMF6
Low
High
Cell abundance

Figure 4. scRNA-seq and ST integration with enhanced-resolution clustering resolve the complex dystrophic muscle architecture and cellular distribution and profiles of myeloid subtypes.

A. Left: H&E images of mouse GAST from 2-mo D2.*mdx* used for ST. Histopathological annotation areas are noted: regenerative muscle (yellow), necrotic/inflammatory lesions (green), healthy muscle (blue). Right: Percentage of spots in the annotated areas. Each section is from a different biological replicate, and each library was obtained from a separate Visium experiment followed by bioinformatic integration to remove batch effects.

B. Enhanced subspot resolution clustering (*BayesSpace*) identified seven spatial clusters (color-coded), which were not resolved by pathologist annotations. The white rectangle highlights a lesion with structured inflammation and regeneration zones.

C. Top marker gene expression after z-score transformation for each spatial cluster. Dot size represents the percentage of subspots expressing the gene.

D. Spatial expression of representative genes coding for markers of each spatial cluster: *Ccl2* and *Ccl7* (LGCs; cluster 2*), Itgax, Mmp12, Trem2*, and *Gpnmb* (resolution-related MFs and GFEMs; cluster 6), *Myog* and *Myh3* (newly regenerating fibers; cluster 1), *Pvalb* and *Tpm3* (healthy muscle; cluster 7), *Col1a1* (ECM; cluster 4) and *Esam* (endothelial cell/vasculature-enriched areas; cluster 3). Note the differential spatial expression patterns in the highlighted region of **4B**.

E. Single-cell transcriptomes derived from $CD45^+$ sorted cells from 2-mo D2.*mdx* GAST. A total number of 4,811 myeloid cells (MFs, monocytes, DCs; *SingleR* automated annotation using the *ImmGen* database) were analyzed. Data are presented as a t-SNE projection to visualize variation in single-cell transcriptomes. The subsampling-based clustering approach (*chooseR)* resolved seven myeloid subsets (color-coded).

F. Top marker genes for the seven identified clusters. Dot size represents the percentage of expressing cells within a group, and color-scale represents the average expression level (row Z-score) across all cells within the cluster.

G. Left: 2D embeddings visualizing cell cycle phases of the 2-mo D2.*mdx* scRNA-seq dataset using t-SNE. NA indicates the number of unassigned cells. Right: 2D embeddings visualizing three subclusters of cycling cells from parent cluster 6 using *VeloViz* embeddings. Cell numbers for each subcluster are indicated. Arrows show velocity projections (*velocyto.R*).

H. Identification of tissue compartments using NMF-based decomposition and 2-mo D2.*mdx* reference immune subtype expression signatures (7). Heatmap of the estimated NMF weights of cell subtypes (rows) across six predicted NMF components (columns), corresponding to the identified cellular compartments. Relative weights normalized across domains for every MF subtype are shown.

I. Spatial plots show cell abundance for each immune cell subtype calculated in **4H**.

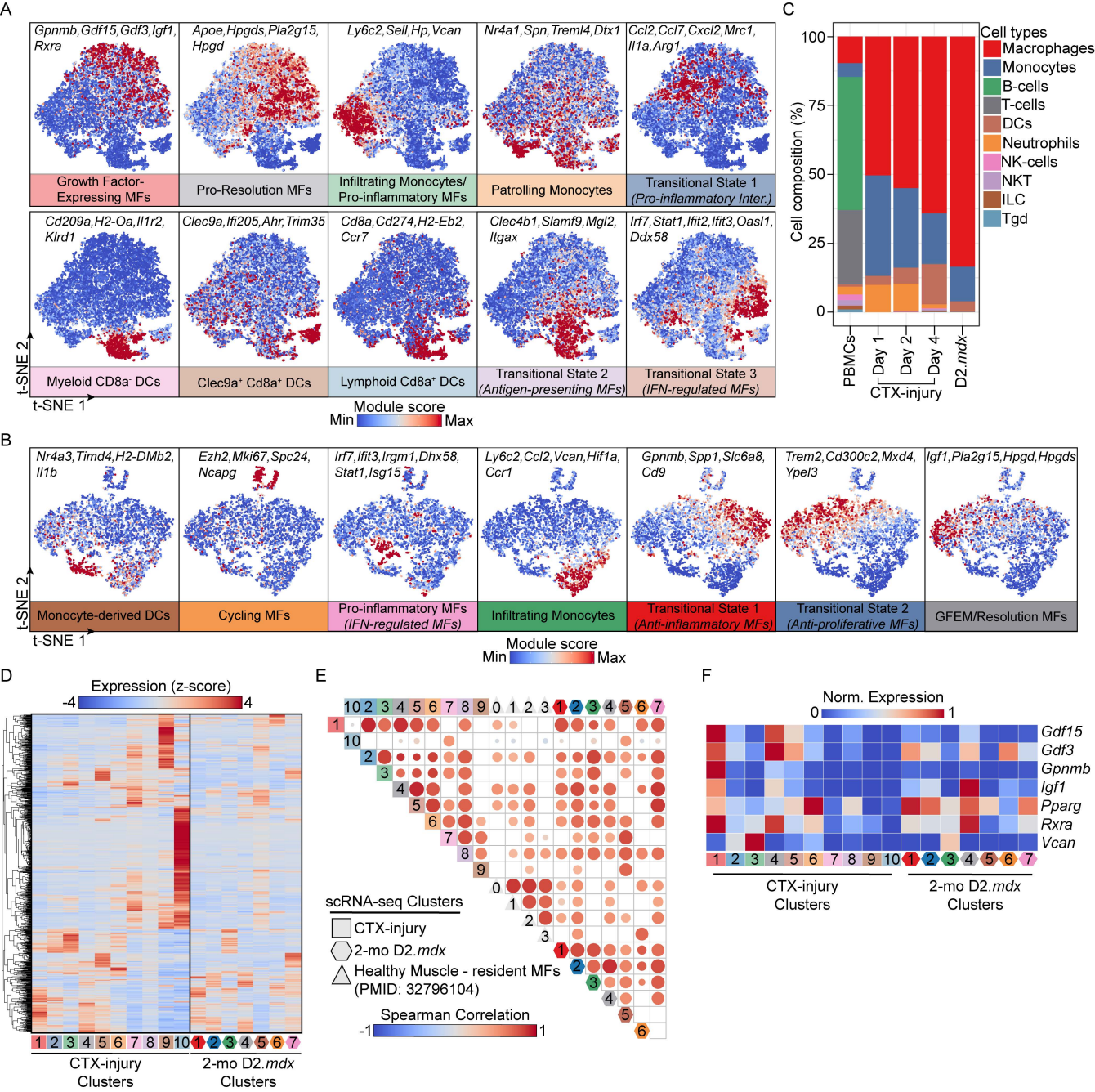
A
Gpnmb, Gdf15, Gdf3, Igf1, Rxra
Growth Factor-Expressing MFs
Apoe, Hpgds, Pla2g15, Hpgd
Pro-Resolution MFs
Ly6c2, Sell, Hp, Vcan
Infiltrating Monocytes/ Pro-inflammatory MFs
Nr4a1, Spn, Treml4, Dtx1
Patrolling Monocytes
Ccl2, Ccl7, Cxcl2, Mrc1, Il1a, Arg1
Transitional State 1 (Pro-inflammatory Inter.)
Cd209a, H2-Oa, Il1r2, Klrd1
Myeloid CD8a- DCs
Clec9a, Ifi205, Ahr, Trim35
Clec9a+ Cd8a+ DCs
Cd8a, Cd274, H2-Eb2, Ccr7
Lymphoid Cd8a+ DCs
Clec4b1, Slamf9, Mgl2, Itgax
Transitional State 2 (Antigen-presenting MFs)
Irf7, Stat1, Ifit2, Ifit3, Oasl1, Ddx58
Transitional State 3 (IFN-regulated MFs)
t-SNE 2
t-SNE 1
Module score
Min
Max
C
Cell composition (%)
100
75
50
25
0
PBMCs
Day 1
Day 2
Day 4
D2.mdx
CTX-injury
Cell types
Macrophages
Monocytes
B-cells
T-cells
DCs
Neutrophils
NK-cells
NKT
ILC
Tgd
B
Nr4a3, Timd4, H2-DMb2, Il1b
Monocyte-derived DCs
Ezh2, Mki67, Spc24, Ncapg
Cycling MFs
Irf7, Ifit3, Irgm1, Dhx58, Stat1, Isg15
Pro-inflammatory MFs (IFN-regulated MFs)
Ly6c2, Ccl2, Vcan, Hif1a, Ccr1
Infiltrating Monocytes
Gpnmb, Spp1, Slc6a8, Cd9
Transitional State 1 (Anti-inflammatory MFs)
Trem2, Cd300c2, Mxd4, Ypel3
Transitional State 2 (Anti-proliferative MFs)
Igf1, Pla2g15, Hpgd, Hpgds
GFEM/Resolution MFs
t-SNE 2
t-SNE 1
Module score
Min
Max
D
Expression (z-score)
-4
4
1 2 3 4 5 6 7 8 9 10 1 2 3 4 5 6 7
CTX-injury Clusters
2-mo D2.mdx Clusters
E
10 2 3 4 5 6 7 8 9 0 1 2 3 1 2 3 4 5 6 7
1
10
2
3
4
5
6
7
8
9
0
1
2
3
1
2
3
4
5
6
scRNA-seq Clusters
CTX-injury
2-mo D2.mdx
Healthy Muscle - resident MFs (PMID: 32796104)
Spearman Correlation
-1
1
F
Norm. Expression
0
1
Gdf15
Gdf3
Gpnmb
Igf1
Pparg
Rxra
Vcan
1 2 3 4 5 6 7 8 9 10 1 2 3 4 5 6 7
CTX-injury Clusters
2-mo D2.mdx Clusters

Figure 5. Infiltrating myeloid cell transcriptomic profile comparison from healthy, acutely injured, and early-stage dystrophic muscle.

A. Module score of gene sets representing functional markers of each myeloid subset visualized with a t-SNE in the CTX-injury time-course scRNA-seq dataset. Genes for each module are indicated.

B. Module score of gene sets representing functional markers of each myeloid subset visualized with a t-SNE in the 2-mo D2.*mdx* scRNA-seq dataset. Genes for each module are indicated.

C. Composition bar plot of the major immune cell types in the *Harmony* integrated dataset (2-mo D2.*mdx* + CTX-injury).

D. Heatmap of top genes in 2-mo D2.*mdx* vs. CTX-injury monocytes, MF and DC subsets.

E. Pairwise Spearman correlation plot of monocytes, MF, and DC subsets identified in 2-mo D2.*mdx*, CTX-injury, and resident muscle MFs from healthy quadriceps (36) (1300 total; *presto* wilcox AUC; logFC>0.5, *p*-adj<0.1, AUC>0.5). The resident MFs are represented according to the following nomenclature chosen by the authors (36): “Cluster 0” (cluster 0), “*Cd209* cluster” (cluster 1), “*Ccr2* cluster” (cluster 2), and “Proliferating cluster” (cluster 3). Color intensity and circle size are proportional to the correlation coefficients. Note (a) the relative uniqueness of resident MFs, (b) the high correlation of pro-inflammatory monocytes (cluster 3) in both CTX and D2.*mdx* datasets, and (c) the high correlation of cycling MFs in D2.*mdx* (cluster 6) with the resident MFs (Proliferating cluster).

F. Heatmap of known regulators of regeneration in 2-mo D2.*mdx* vs. CTX-injury monocyte, MF, and DC subsets.

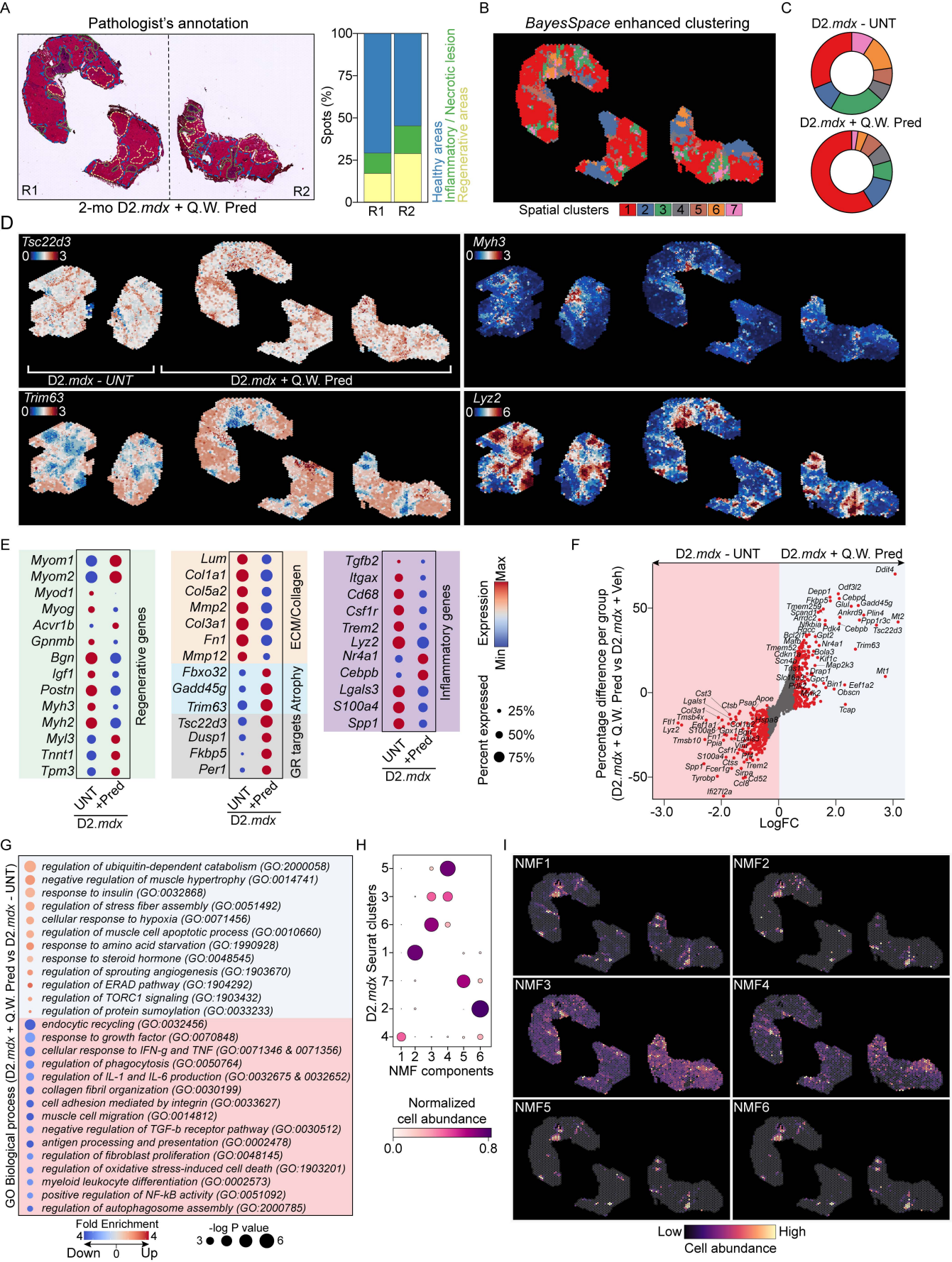
A
Pathologist's annotation
R1
R2
2-mo D2.mdx + Q.W. Pred
Spots (%)
100
75
50
25
0
R1
R2
Healthy areas
Inflammatory / Necrotic lesion
Regenerative areas
B
BayesSpace enhanced clustering
Spatial clusters
1 2 3 4 5 6 7
C
D2.mdx - UNT
D2.mdx + Q.W. Pred
D
Tsc22d3
0 3
Myh3
0 3
D2.mdx - UNT
D2.mdx + Q.W. Pred
Trim63
0 3
Lyz2
0 6
E
Myom1
Myom2
Myod1
Myog
Acvr1b
Gpnmb
Bgn
Igf1
Postn
Myh3
Myh2
Myl3
Tnnt1
Tpm3
Regenerative genes
Lum
Col1a1
Col5a2
Mmp2
Col3a1
Fn1
Mmp12
ECM/Collagen
Fbxo32
Gadd45g
Trim63
Tsc22d3
Dusp1
Fkbp5
Per1
GR targets Atrophy
UNT
+Pred
D2.mdx
Tgfb2
Itgax
Cd68
Csf1r
Trem2
Lyz2
Nr4a1
Cebpb
Lgals3
S100a4
Spp1
Inflammatory genes
UNT
+Pred
D2.mdx
Expression
Max
Min
Percent expressed
25%
50%
75%
F
D2.mdx - UNT
D2.mdx + Q.W. Pred
Percentage difference per group
(D2.mdx + Q.W. Pred vs D2.mdx + Veh)
50
0
-50
-3.0
-2.0
0
2.0
3.0
LogFC
Ddit4
Odf3l2
Depp1
Cebpd
Fkbp5
Tmem233
Gadd45g
Glul
Scand1
Ankrd9
Plin4
Mt2
Arrdc2
Ppp1r3c
Mfsd6
Pdk4
Cebpb
Tsc22d3
Rrad
Bcl2l11
Gpt2
Mafb
Nr4a1
Trim63
Tmem52
Bola3
Cdkn1a
Klf1c
Scn4b
Map2k3
Trib3
Drap1
Mt1
Slc16a3
Gpc1
Pdk4
Bin1
Eef1a2
Ank2
Obscn
Csf3
Lgals1
Ctsb
Psap
Apoe
Col3a1
Tcap
Tmsb4x
Flt1
Eef1a1
Col1a1
Lyz2
S100a6
Cpx1
Bgn
Hspa8
Tmsb10
Fn1
Lgals3
Tpm1
Csf1r
Vim
S100a4
Ctss
Trem2
Spp1
Fcer1g
Sirpa
Cd52
Tyrobp
Ccl6
Ifi27l2a
G
GO Biological process (D2.mdx + Q.W. Pred vs D2.mdx - UNT)
regulation of ubiquitin-dependent catabolism (GO:2000058)
negative regulation of muscle hypertrophy (GO:0014741)
response to insulin (GO:0032868)
regulation of stress fiber assembly (GO:0051492)
cellular response to hypoxia (GO:0071456)
regulation of muscle cell apoptotic process (GO:0010660)
response to amino acid starvation (GO:1990928)
response to steroid hormone (GO:0048545)
regulation of sprouting angiogenesis (GO:1903670)
regulation of ERAD pathway (GO:1904292)
regulation of TORC1 signaling (GO:1903432)
regulation of protein sumoylation (GO:0033233)
endocytic recycling (GO:0032456)
response to growth factor (GO:0070848)
cellular response to IFN-g and TNF (GO:0071346 & 0071356)
regulation of phagocytosis (GO:0050764)
regulation of IL-1 and IL-6 production (GO:0032675 & 0032652)
collagen fibril organization (GO:0030199)
cell adhesion mediated by integrin (GO:0033627)
muscle cell migration (GO:0014812)
negative regulation of TGF-b receptor pathway (GO:0030512)
antigen processing and presentation (GO:0002478)
regulation of fibroblast proliferation (GO:0048145)
regulation of oxidative stress-induced cell death (GO:1903201)
myeloid leukocyte differentiation (GO:0002573)
positive regulation of NF-kB activity (GO:0051092)
regulation of autophagosome assembly (GO:2000785)
Fold Enrichment
4
4
Down
0
Up
-log P value
3
6
H
D2.mdx Seurat clusters
5
3
6
1
7
2
4
1 2 3 4 5 6
NMF components
Normalized
cell abundance
0.0
0.8
I
NMF1
NMF2
NMF3
NMF4
NMF5
NMF6
Low
High
Cell abundance

Figure 6. ST organization of dystrophic muscle upon intermittent prednisolone treatment.

A. Left: H&E images of GAST from 2-mo D2.*mdx* mice treated weekly (Q.W.) for 4 weeks with prednisolone, used for ST. Histopathological annotation areas: regenerative muscle (yellow), necrotic/inflammatory lesions (green), healthy muscle (blue). Right: Percentage of spots in annotated areas. Each section is from a different biological replicate, and each library was obtained from a separate Visium experiment followed by bioinformatic integration to remove batch effects.

B. Enhanced subspot resolution clustering (*BayesSpace*) identified seven meaningful spatial clusters (color-coded) unresolved by pathologist annotations.

C. Comparison of the spatial cluster (color-coded) sub-spot composition in untreated D2.*mdx* and D2.*mdx* treated Q.W. with prednisolone (UNT=Untreated).

D. Spatial expression of representative GR targets, regenerative muscle, inflammation, and atrophy marker genes is shown. *Myh3* indicates newly regenerating fibers, *Tsc22d3* GR target engagement, *Lyz2* inflammatory myeloid cells, and *Trim63* atrophy-inducing pathways.

E. Representative DEGs in untreated D2.*mdx* vs. D2.*mdx*+Q.W. Pred comparison, grouped in functional categories. Dot size represents the percentage of spots within a treatment group.

F. Unbiased global tissue-wide DGE of all spots in D2.*mdx*+Q.W. Pred vs. D2.*mdx*-UNT (red dots indicate significant DEGs; $p<0.05$, logFC>1). Top DEG names are indicated.

G. Gene ontology pathway enrichment analysis of the DEGs in D2.*mdx*+Q.W. Pred *vs.* D2.*mdx*-UNT ST datasets. Top significant up- and down-regulated pathways are shown ($p<0.001$, fold enrichment >2). Grey box: enriched GO terms with Pred-treatment; red box: downregulated terms with Pred-treatment.

H. Identification of tissue compartments in D2.*mdx*+Q.W. Pred-treated ST samples using NMF-based decomposition and 2-mo D2.*mdx* reference immune subtype expression signatures (7). Dot plot of estimated NMF weights of cell subtypes (rows) across six predicted NMF components (columns) corresponding to the identified cellular domains. Relative weights normalized across components for every MF subtype are shown.

I. Spatial plots show cell abundance for each immune cell type calculated in **6H**.

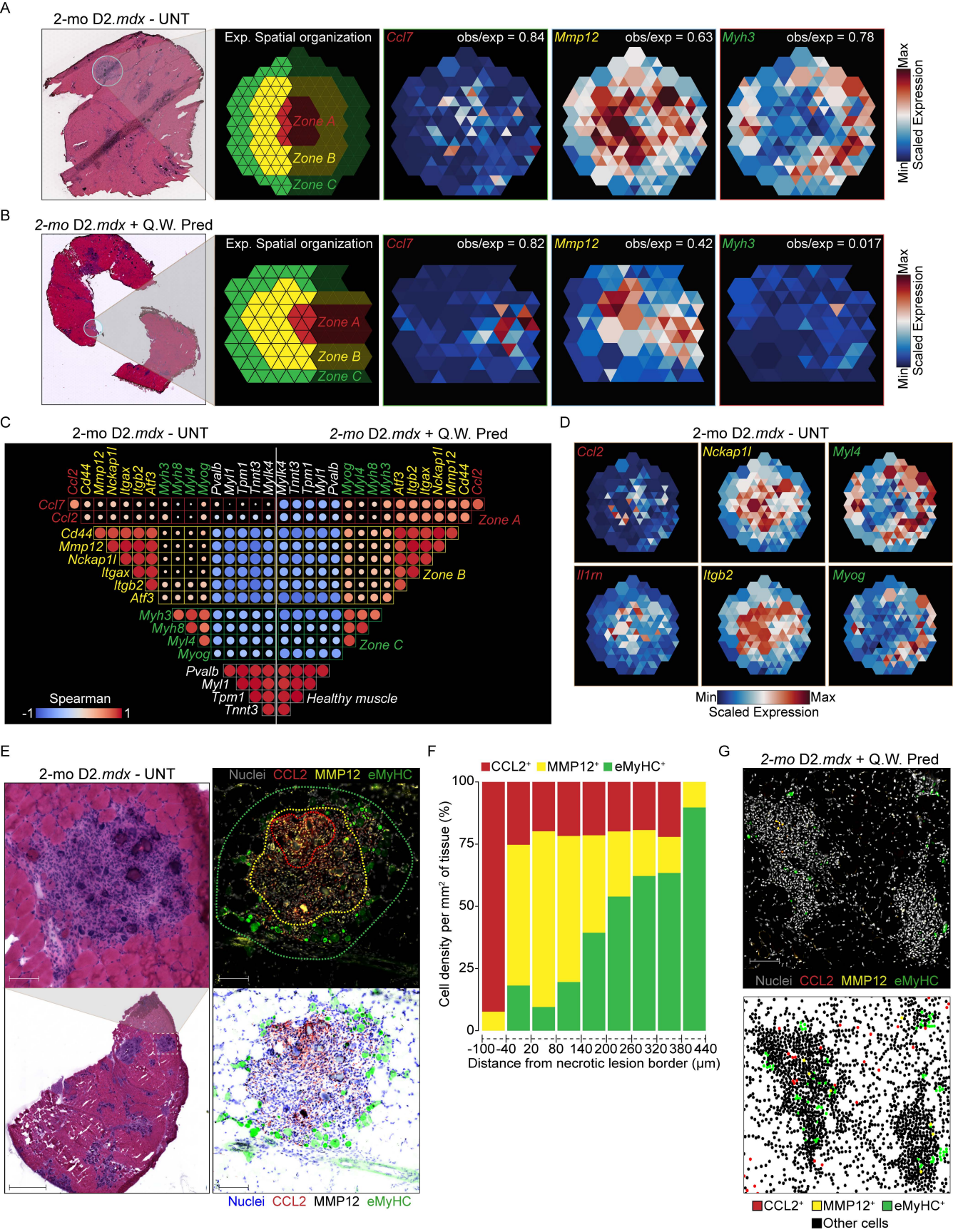
A
2-mo D2.mdx - UNT
Exp. Spatial organization
Zone A
Zone B
Zone C
Ccl7
obs/exp = 0.84
Mmp12
obs/exp = 0.63
Myh3
obs/exp = 0.78
Max
Min
Scaled Expression
B
2-mo D2.mdx + Q.W. Pred
Exp. Spatial organization
Zone A
Zone B
Zone C
Ccl7
obs/exp = 0.82
Mmp12
obs/exp = 0.42
Myh3
obs/exp = 0.017
Max
Min
Scaled Expression
C
2-mo D2.mdx - UNT
2-mo D2.mdx + Q.W. Pred
Ccl2
Cd44
Mmp12
Nckap1l
Itgax
Itgb2
Atf3
Myh3
Myh8
Myl4
Myog
Pvalb
Myl1
Tpm1
Tnnt3
Mylk4
Zone A
Zone B
Zone C
Healthy muscle
Spearman
-1
1
D
2-mo D2.mdx - UNT
Ccl2
Nckap1l
Myl4
Il1rn
Itgb2
Myog
Min
Max
Scaled Expression
E
2-mo D2.mdx - UNT
Nuclei CCL2 MMP12 eMyHC
Nuclei CCL2 MMP12 eMyHC
F
CCL2+ MMP12+ eMyHC+
Cell density per mm2 of tissue (%)
100
75
50
25
0
-100 -40 20 80 140 200 260 320 380 440
Distance from necrotic lesion border (µm)
G
2-mo D2.mdx + Q.W. Pred
Nuclei CCL2 MMP12 eMyHC
CCL2+ MMP12+ eMyHC+
Other cells

Figure 7. RIZs are disrupted by GC treatment in early-stage dystrophy.

A. Magnified view of representative structures and RIZs in untreated 2-mo D2.*mdx* muscles. Zone A represents the center of an inflammatory lesion occupied by LGCs ($Ccl7^+$); Zone B is occupied by a gradient of resolution-related MFs ($Mmp12^+$) and GFEMs; and Zone C represents the regeneration zone marked by developing myofibers ($Myh3^+$). The correlation of observed/expected zone organization is quantified per subspot. H&E data have been previously presented in **4A** and provide the location and context for the magnified feature plots.

B. Abnormal tissue zones in 2-mo D2.*mdx*+Q.W. Pred animals. Note the disintegration/absence of regenerating fibers (*Myh3*+) in Zone C. H&E images have been previously presented in **6A** and provide the location and context for the magnified feature plots.

C. Global subspot correlation (Spearman) of spatial gene expression in 2-mo D2.*mdx*-UNT and 2-mo D2.*mdx*+Q.W. Pred samples. Higher correlation in Pred samples suggests a collapse and re-arrangement of inflammatory (Zones A, B) and regenerative (Zone C) zones (color-coded).

D. Example of RIZs formed with alternative markers.

E. Representative H&E region of RIZs in 2-mo D2.*mdx* GAST validated by IF. The MF subtypes and zones were visualized with IF (bottom panel shows the absorbed signal) for CCL2 (Zone A), MMP12 (Zone B), and eMyHC (Zone C). Dotted lines indicate the zones and interface layer (red; necrotic lesion) selected for cell density quantification in **7F**. Scale bars: 1 mm (lower left) and 100 μm (others).

F. Stacked bar histogram of $CCL2^+$, $MMP12^+$, and $eMyHC^+$ cell density inside (-1 to -100 μm) and outside (+1 to +440 μm) the necrotic boundary in **7E**.

G. Representative IF region with two inflammatory lesions in 2-mo D2.*mdx*+Q.W. Pred GAST samples. MF subtypes and regenerating fibers were visualized as in **7E**. Bottom panel indicates the cell density and distribution. Scale bar: 100 μm.

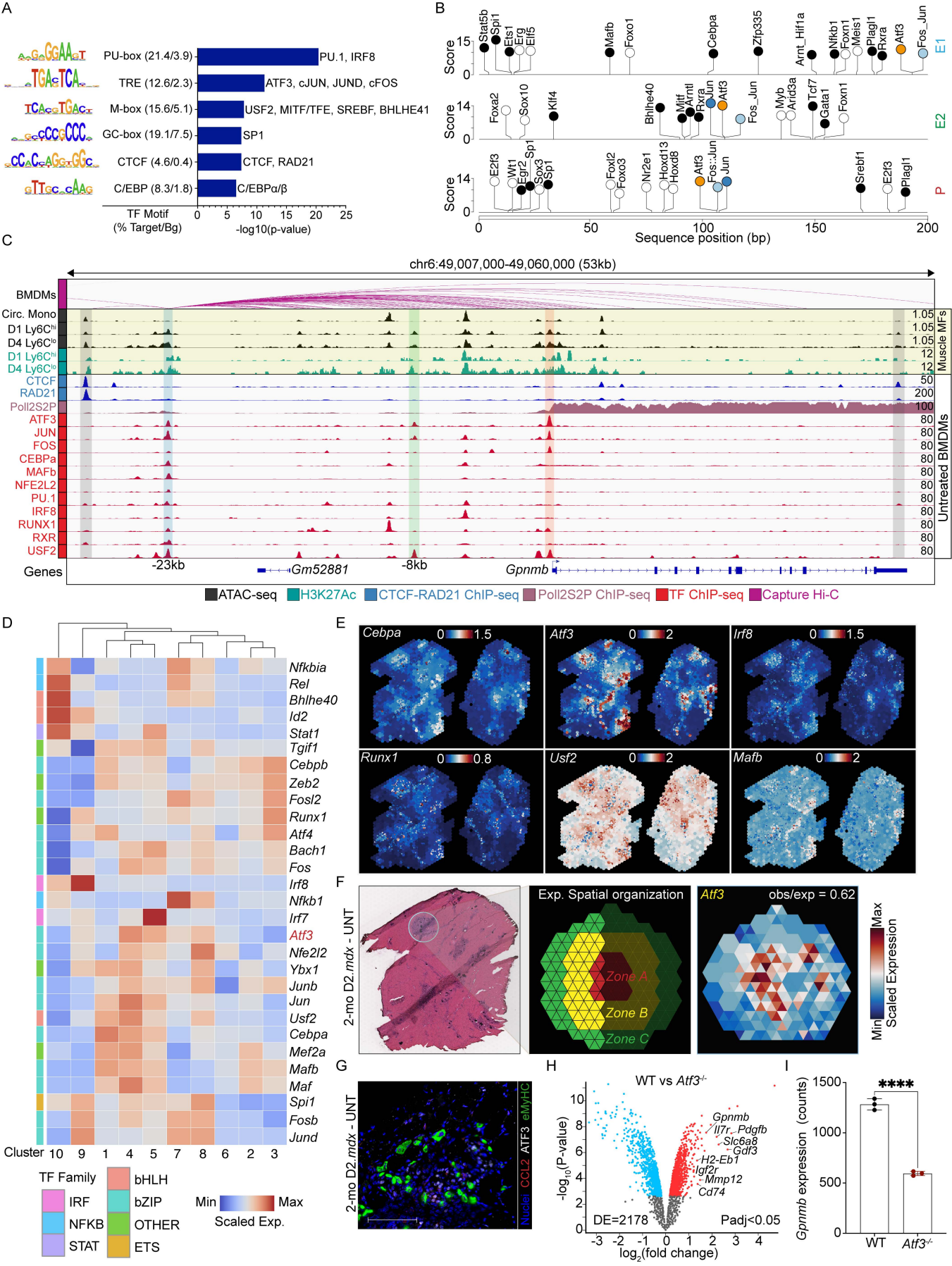
A
PU-box (21.4/3.9)
PU.1, IRF8
TRE (12.6/2.3)
ATF3, cJUN, JUND, cFOS
M-box (15.6/5.1)
USF2, MITF/TFE, SREBF, BHLHE41
GC-box (19.1/7.5)
SP1
CTCF (4.6/0.4)
CTCF, RAD21
C/EBP (8.3/1.8)
C/EBPα/β
TF Motif (% Target/Bg)
-log10(p-value)
B
Score
Sequence position (bp)
E1
E2
P
C
chr6:49,007,000-49,060,000 (53kb)
BMDMs
Circ. Mono
D1 Ly6C^hi
D4 Ly6C^lo
Muscle MFs
Untreated BMDMs
CTCF
RAD21
Pol2S2P
ATF3
JUN
FOS
CEBPa
MAFb
NFE2L2
PU.1
IRF8
RUNX1
RXR
USF2
Genes
-23kb
Gm52881
-8kb
Gpnmb
ATAC-seq
H3K27Ac
CTCF-RAD21 ChIP-seq
Pol2S2P ChIP-seq
TF ChIP-seq
Capture Hi-C
D
Nfkbia
Rel
Bhlhe40
Id2
Stat1
Tgif1
Cebpb
Zeb2
Fosl2
Runx1
Atf4
Bach1
Fos
Irf8
Nfkb1
Irf7
Atf3
Nfe2l2
Ybx1
Junb
Jun
Usf2
Cebpa
Mef2a
Mafb
Maf
Spi1
Fosb
Jund
Cluster
TF Family
IRF
NFKB
STAT
bHLH
bZIP
OTHER
ETS
Min
Max
Scaled Exp.
E
Cebpa
Atf3
Irf8
Runx1
Usf2
Mafb
F
2-mo D2.mdx - UNT
Exp. Spatial organization
Zone A
Zone B
Zone C
Atf3
obs/exp = 0.62
Max
Min
Scaled Expression
G
2-mo D2.mdx - UNT
Nuclei
CCL2
ATF3
eMyHC
H
WT vs Atf3-/-
-log10(P-value)
log2(fold change)
Gpnmb
Il7r
Pdgfb
Slc6a8
Gdf3
H2-Eb1
Igf2r
Mmp12
Cd74
DE=2178
Padj<0.05
I
Gpnmb expression (counts)
****
WT
Atf3-/-

Figure 8. ATF3 directly regulates a GFEM-like transcriptional program.

A. *De novo* motif enrichments around the TSSs of GFEM-associated genes. ATAC-seq peaks of day 4 post-CTX Ly6C^{low} repair muscle MFs within 50 kb of TSSs were selected as input. Detected motif matrices, *p*-values, and background are shown.

B. Predicted scores and motif map of 2 distal enhancers (E1, E2) and 1 proximal (P) site around the *Gpnmb* locus, selected based on their muscle MF-specific chromatin openness (ATAC-seq). Open and closed circles indicate the absence or presence of corresponding TF mRNA, respectively. Motifs of ATF3 and co-binding partner JUN are highlighted.

C. Genome browser view of the *Gpnmb* locus indicating capture Hi-C (in naïve BMDMs), ATAC-seq (blood monocyte and muscle-infiltrating MFs; normalized scale), and ChIP-seq (in naïve BMDMs and muscle-infiltrating MFs) for indicated TFs, active transcription histone marks (H3K27Ac), and elongating Polymerase II (S2P). CTCF and RAD21-defined transcriptional unit boundaries, distal (E1; green, E2; blue) and proximal (P; red) *Gpnmb*-associated regulatory elements and track scales are indicated.

D. Heatmap of the highest expressed TFs (decile-filtered) in the myeloid subtypes of the CTX scRNA-seq dataset (**Fig. 2F**). Hierarchical clustering, and average log-normalized expression values are shown. *Atf3* is highlighted.

E. Spatial expression feature plots of top TFs with detected binding in the regulatory elements in the D2.*mdx* samples.

F. Magnified view of *Atf3* spatial expression in representative RIZs in untreated 2-mo D2.*mdx* muscles. The correlation of observed/expected zone organization is quantified per subspot for each Zone and indicates an overlap of *Atf3* with Zone B. Data in this figure (left and middle) have been previously presented in **4A** and **7A**, respectively and provide the location and context for the magnified feature plot and expected spatial organization.

G. IF region of a lesion in 2-mo D2.*mdx* GAST muscle. MF subtypes were visualized with CCL2 (red; Zone A) and ATF3 (yellow; Zone B), and regenerating fibers with eMyHC (green; Zone C). Scale bar: 100 μm.

H. Volcano plot showing the differentially expressed genes in the *Atf3*$^{-/-}$ naïve BMDMs (p<0.01, FDR<0.01). Number of DEGs and gene labels of GFEM-predicted markers among top DEGs are shown.

I. *Atf3* mRNA expression in WT and *Atf3*$^{-/-}$ naïve BMDMs (n=3; unpaired t-test, p<0.0001).

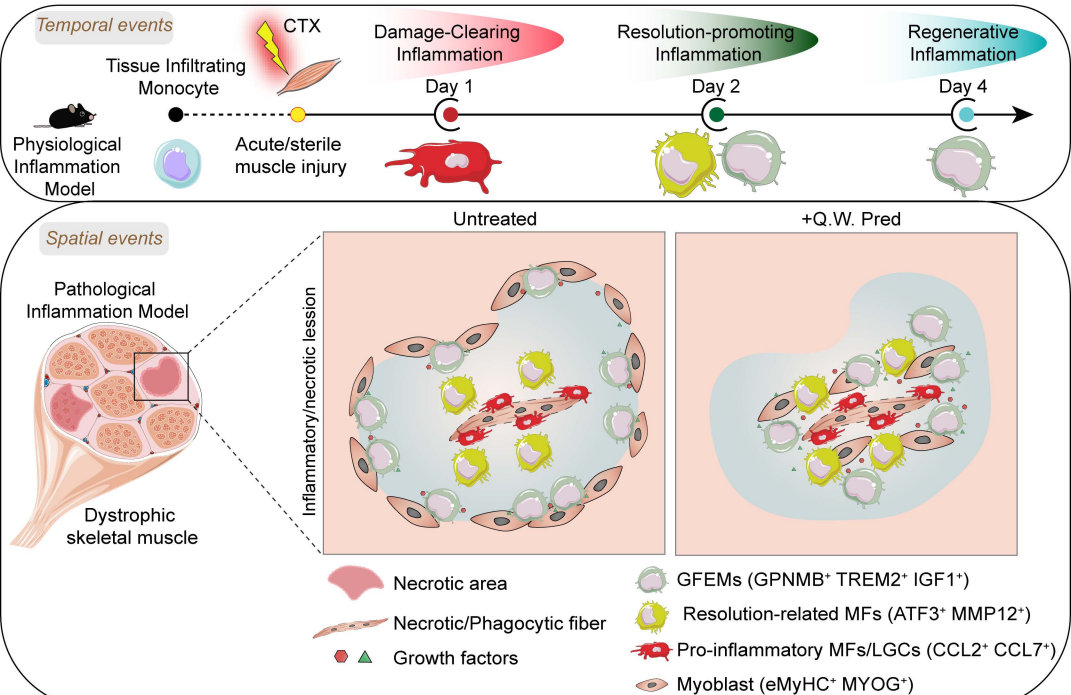
Temporal events
CTX
Tissue Infiltrating Monocyte
Physiological Inflammation Model
Acute/sterile muscle injury
Damage-Clearing Inflammation
Day 1
Resolution-promoting Inflammation
Day 2
Regenerative Inflammation
Day 4
Spatial events
Pathological Inflammation Model
Dystrophic skeletal muscle
Untreated
+Q.W. Pred
Inflammatory/necrotic lesion
Necrotic area
Necrotic/Phagocytic fiber
Growth factors
GFEMs (GPNMB+ TREM2+ IGF1+)
Resolution-related MFs (ATF3+ MMP12+)
Pro-inflammatory MFs/LGCs (CCL2+ CCL7+)
Myoblast (eMyHC+ MYOG+)

Graphical Abstract

Representation of the principles of regenerative inflammation: The temporal order of MF subsets identified in a synchronous and homogenous injury model corresponds to the spatial arrangement of regenerative tissue zones in the complex dystrophic muscle. The multilayered RIZs are sensitive to intermittent GC treatment. LGCs: Langhans Giant Cells, CTX: Cardiotoxin, QW+Pred: once weekly prednisolone, GFEMs: Growth Factor-Expressing Macrophages, MFs: macrophages.